



Thermal lensing and photoacoustics as potential tools for nanomaterial characterization: a review

M. S. Swapna¹, S. Sankararaman², and D. Korte^{1,*}

¹ University of Nova Gorica, Vipavska 13, 5000 Nova Gorica, Slovenia

² Department of Optoelectronics, University of Kerala, Trivandrum, Kerala 695581, India

Received: 8 March 2024

Accepted: 14 May 2024

© The Author(s), 2024

ABSTRACT

This comprehensive review highlights the versatile applications of photothermal techniques, particularly thermal lens spectrometry (TLS) and photoacoustic spectrometry (PAS), in the field of nanomaterials characterization. TLS is an effective technique in the trace detection of different compounds in liquid samples, photodegradation studies, and analysis of photocatalytic reaction rate, as well as the study of molecular dynamics, impacting both environmental and catalytical research. It enables the optimization of thermal diffusivity in soot nanofluids and offers insights into seed germination and plant yield enhancement in nanobio-photonics. The review also explores the thermal and elastic characterization of Fe₂O₃ polymorphs by photoacoustic spectroscopy (PAS). Investigating the metal mirror demonstrates PAS's efficacy in determining its reflection coefficient and thermal diffusivity. ZnO nanoparticles' strong absorption on diatomite surfaces is revealed through PAS, emphasizing their effectiveness in light absorption enhancement. Furthermore, PA techniques address working frequency limitations in studying silicon-based nanomaterials. Thus, thermal lens and photoacoustic spectroscopy assume pivotal roles in unveiling the nuanced attributes of various nanostructured materials, thereby propelling advancements in the realms of science and technology.

Introduction

Nanomaterials (NMs) are entities possessing external dimensions or internal structures that fall within the dimensional range of 1–100 nm, engendering novel attributes. They exhibit a taxonomical stratification based on their morphological configurations. Among these, the foremost class comprises nanoparticles

(NPs), wherein all three external dimensions reside within the nanoscale domain and exhibit minimal dissimilarity. Conversely, nanofibers (NFs), nanotubes (NTs), and nanorods (NRs) feature two dimensions below 100 nm, while nanoplates (NPLs), nanosheets (NSHs), and nanoribbons (NRBs) manifest a solitary external dimension in the nanoscale [1, 2]. In the context of the latter two NM groupings, their

Handling Editor: Pedro Camargo.

Address correspondence to E-mail: Dorota.Korte@ung.si

<https://doi.org/10.1007/s10853-024-09773-4>

Published online: 25 May 2024

supplementary dimensions are markedly expansive relative to those within the nanoscale. An additional cohort of nanomaterials comprises nanostructures (NSs), encompassing nanocomposites (NCs), nanofoams (NFMs), nanoporous materials (NPMs), and nanocrystalline materials (NCMs) [3]. NCs denote solid constructs characterized by including at least one phase possessing one, two, or three dimensions within the nanoscale spectrum. NFMs are either liquid or solid matrices imbued with gaseous elements, wherein a requisite phase within NFMs must exhibit attributes conforming to the criteria of nanomaterials. NPMs assume the form of voluminous solid phases housing voids that exhibit open and/or closed porosity configurations, with pore dimensions confined to the nanoscale. NCMs signify amorphous matrix materials wherein interstices are replete with a substantial proportion of crystal grains (crystallites) having dimensions beneath 100 nm.

Owing to their nanoscale dimensions, NMs exhibit distinct chemical, physical, optical, and mechanical properties that differ from bulk materials [1–3]. Their elevated surface-to-volume ratio positions them as significant catalysts, pharmaceuticals, sensors, and actuation systems while also serving as advanced conductive materials due to their low percolation threshold [3–8]. With increased hardness, NMs are utilized as potential protective layers, and their enhanced resistivity and reliability render them attractive for electronics, optoelectronics, and photonics applications [6, 9, 10]. Moreover, NMs display improved atomic transport kinetics and lower melting temperatures, rendering them promising for applications in batteries, solar cells, energy storage, and conversion devices [11–13], among other industrial and life science realms. Consequently, diverse NM forms are under intensive investigation. Characterization techniques [2] include transmission electron (TEM) and scanning electron (SEM) microscopy, Fourier transform infrared (FTIR), X-ray diffraction (XRD), and various spectroscopic techniques for examining morphological, structural, and mechanical properties. In contrast, atomic force microscopy (AFM), piezoresponse force microscopy (PFM), and other methods assess electrical, physicochemical, piezoelectric, and magnetic properties. These measurements are complemented by simulation methods like density functional theory and finite elemental analysis [14, 15], which are especially relevant for understanding NM interactions with biological and environmental systems.

The comprehensive characterization and determination of nanomaterials (NMs) properties constitute a multifaceted challenge crucial for harnessing their transformative potential in contemporary technologies. The challenge is to obtain NMs with well-controlled nanoscale-related properties, which requires developing new measurement techniques that ensure high precision NMs characterization and their properties determination together with the correlation of the parameters with the NMs nanostructure. Techniques that are perspective in NM characterization are those based on the photothermal (PT) effect [8, 16–20]. The PT effect is the consequence of light absorption from the excitation radiation (ER) illuminating the examined sample, followed by a number of radiationless de-excitation processes. This leads to the generation of temperature oscillations (TOs) in the sample and its surroundings that further induce changes in temperature, pressure, and refractive index of the medium as well as in the illuminated sample as deformation of its surface. TOs carry information about the examined sample's thermal and optical properties, which are determined by its internal structure and transport properties [21, 22]. Several photothermal techniques have been developed to monitor the changes induced in the sample and its surrounding medium by TOs. The temperature rise is measured by photopyroelectric spectroscopy (PPES) and calorimetry (PPEC) using a pyroelectric sensor in direct thermal contact with the sample [23], the pressure change in gas above the examined sample is detected by photoacoustic spectrometry (PAS) [24], the changes in refractive index or sample surface deformation are sensed by beam deflection spectrometry (BDS) [24, 25], the thermal emission from examined sample is by photothermal radiometry (IR) [21, 26], whereas the change in optical properties is by thermal lens spectrometry (TLS) or microscopy (TLM) [27–29].

Photothermal techniques offer a suite of advantages over conventional methods, encompassing elevated sensitivity and broad applicability across an extensive spectrum of sample types, spanning from bulk materials to diverse nanomaterials in various configurations, including fluids (gases, liquids), solids, thin films, multilayered structures, and complex composites while accommodating both transparent and opaque specimens [21, 24]. These methodologies additionally facilitate scrutinizing diverse chemical reactions, non-radiative relaxation processes, photoinduced phenomena, and events linked to phase transitions. The

PT techniques (TLS and PAS) provide nondestructive means for probing nanomaterials' internal structure, composition, and thermal properties, even at low concentrations or in small quantities [30]. They also enable real-time monitoring and dynamic analysis, shedding light on the stability, reactivity, and performance of nanomaterials under different conditions. TLS and PA methods can be seamlessly integrated with other analytical techniques, such as spectroscopy and microscopy, to provide complementary information and a more comprehensive understanding of nanomaterial properties. Also, these techniques require minimal sample quantities, making them ideal for studying delicate or valuable nanomaterials while minimizing waste and resource consumption. Both techniques have the potential for imaging applications, allowing for the spatial mapping of nanomaterial distributions and properties within complex matrices. In the context of this study, the objective is to furnish a succinct overview of the utilization of prominent photothermal techniques, such as thermal lens spectrometry (TLS) and photoacoustic spectrometry (PAS), for characterizing nanomaterials (NMs), with a focus on elucidating their merits and constraints pertinent to specific applications.

Methods

Thermal lens spectrometry and applications

Photothermal phenomena occur when materials absorb photons, which then excite molecules, leading to non-radiative de-excitation and the release of energy in the form of heat within the sample. This liberated heat induces changes in density and refractive index, providing insights into the diverse physical properties of the material. In liquid samples, these refractive index variations generate a lensing effect. When a sample is irradiated by a periodically modulated laser excitation light (ER), the absorbed energy produces a refractive index gradient (RIG), mimicking a diverging lens within the medium known as the thermal lens (TL). Detection of the RIG entails utilizing two distinct methods—the single-beam and dual-beam configurations [21, 31, 32]. In the dual-beam approach, a probe beam (PB) laser is employed to discern the RIG induced by the pump beam (ER), whereas the single-beam configuration relies on variations in the intensity of ER to convey information about the RIG within the

TL region. For optimal signal acquisition in TLS, the sample's positioning is determined experimentally, aligning it approximately 3.5 times the confocal distance (Z_c) beyond the waist of the probe beam [33]. Under these conditions, the changes in relative intensity of the probe beam, stemming from its interaction with the thermal lens, can be expressed as per Eq. (1) [34, 35].

$$\Delta I/I = 2.303EA + (2.303EA)^2/2 + \dots \quad (1)$$

where A is the absorption of the sample, and the enhancement factor relative to the transmission measurements E is given by [31, 35]:

$$E = -P(dn/dT)/1.91\lambda k \quad (2)$$

where λ is the PB wavelength, P is the excitation laser power, $Z_c = 2\pi a^2/\lambda$ is the confocal distance, and a is the PB radius. For low-concentration or weak absorbing species resulting in $A < 0.1$, the second term in Eq. (1) can be neglected. The TLS signal is then directly proportional to the excitation power, absorbance, and enhancement factor of the sample, which enables this technique to be used as a highly sensitive method for determining chemical species at deficient concentrations.

Trace detection of silver NPs

Thermal lens spectrometry (TLS) was employed to monitor the quality of drinking and surface water samples containing colloidal silver nanoparticles (Ag^0 NPs) and to achieve detection limits that are compliant with desired water standards [36]. Investigation into the interaction between a silver salt solution and typical water ions during silver nanoparticle formation was also conducted by various researchers [37, 38]. Colloidal silver NPs, encompassing ionic silver particles, compounds, or colloids suspended in water, exhibit antiseptic, antibacterial, and antimicrobial properties, serving as alternative medical remedies and dietary supplements for internal and external use [39, 40]. Ag^0 NPs at 0.5 mg/L concentration have been utilized to disinfect drinking water on the International Space Station (ISS), owing to their effectiveness against various bacteria and sustained presence in water [41]. However, their residual efficacy is limited due to slow reactions in organic matter elimination. Ag^0 NPs are toxic in higher amounts, causing skin discoloration, silver deposition in the eyes, and severe

health issues [42]. Their ingestion can also interfere with medication absorption. Recommended for germicidal efficacy at 0.025–0.075 mg/L, maximum contamination levels (MCL) range from 0.05 to 0.10 mg/L in different countries and 0.2–0.5 mg/L for space missions. The application of colloidal silver NPs for disinfection, developed by the National Aeronautics and Space Administration, European Space Agency, and World Health Organization over decades, necessitates a sensitive water quality monitoring system for effective implementation.

To facilitate real-time production and detection of silver nanoparticles through the chemical reduction of silver ions from AgNO_3 by NaBH_4 , a flow injection analysis (FIA) system was integrated with a thermal lens spectrometric detection (TLS) unit [36]. The plasmon resonance peak observed in the absorption spectrum at 400 nm in the visible spectrum indicated the formation of Ag^0 NPs with an average diameter ranging from 4 to 40 nm and spherical shape. A pronounced shoulder in the spectra at higher Ag^0 NPs concentrations (2 mg/L and above) indicated the

presence of a broader nanoparticle size distribution and the formation of aggregates. These findings were corroborated by dynamic light scattering and scanning electron microscopy (SEM) measurements. The SEM images of the synthesized NPs are shown in Fig. 1 [36]. The use of FIA in combination with TLS enables avoiding the use of NP stabilizers, which can interfere with the metal surface and influence the results of analysis [36, 43].

A self-constructed FIA system with a dual-beam TLS detection unit, shown in Fig. 2, was utilized to identify Ag^0 NPs in water. The FIA system incorporates two HPLC pumps: one for delivering the reducing reagent and the other for transporting the Ag^+ standard solutions through a metal-free injection valve equipped with sample loops. These solutions are mixed in a Teflon tubing coil to synthesize silver particles, which are then directed into the flow-through detection cell. The carrier and reductant flow at 0.3 mL/min each results in a combined flow rate of 0.6 mL/min and a post-mix reductant concentration of 0.3 mM. Silver colloids are generated by injecting

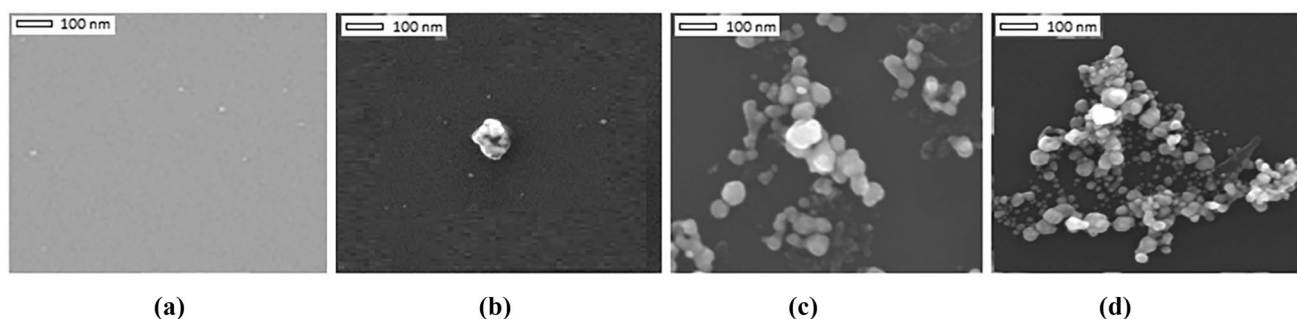
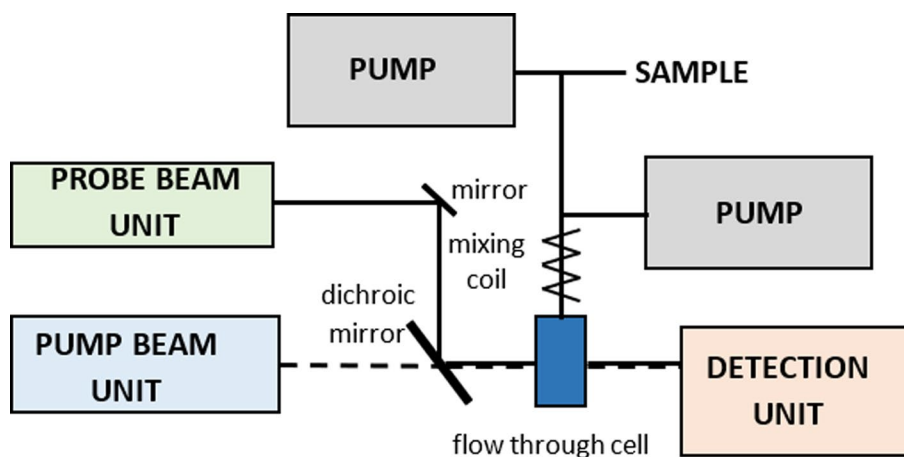


Figure 1 Scanning electron micrographs of the synthesized Ag^0 NPs at **a** 50 ng mL^{-1} , **b** 1 µg mL^{-1} , **c** 5 µg mL^{-1} , **d** 15 µg mL^{-1} [36].

Figure 2 FIA setup with TLS detection unit.



silver ions into a 0.6 mM NaBH₄ solution at pH 12.5. In the TLS detection system, temperature gradients induced in the sample by the modulated pump beam (Krypton laser operating at 407 nm) were probed by a He–Ne laser of 2 mW output power at 632.8 nm and monitored by a pin photodiode placed behind a pinhole and an interference filter, and connected to a lock-in amplifier and a PC. The beams are focused and directed by lenses and mirror onto a dichroic mirror that overlaps them and guides them into a flow-through detection cell with a 1 cm optical pathway and 8 μL volume before reaching the detector. Measurements were optimized using Yates' algorithm and the normal probability plot. The highest signal response (peak height) with the least standard deviation was attained using a 0.6 mM NaBH₄ concentration at pH 12.5, along with an overall flow rate of 0.6 mL/min for carrier and reductant. Further refinement was performed, varying sample loop sizes from 10 to 500 μL and mixing coil lengths from 50 to 75 cm. Optimal conditions were determined as a 100 μL sample loop and a 75 cm mixing coil, offering maximum peak height while maintaining low peak dispersion. Therefore, the optimized setup consisted of a 0.3 mL/min flow rate for both the carrier and reductant, a 100 μL injection loop, a 0.6 mM NaBH₄ concentration at pH 12.5, and a 75 cm mixing coil with a 1 mm internal diameter.

In the study, TLS signal values were acquired through online generation of Ag⁰ NPs, involving triplicate injections of silver sample solutions into water. The obtained values were averaged as peak heights

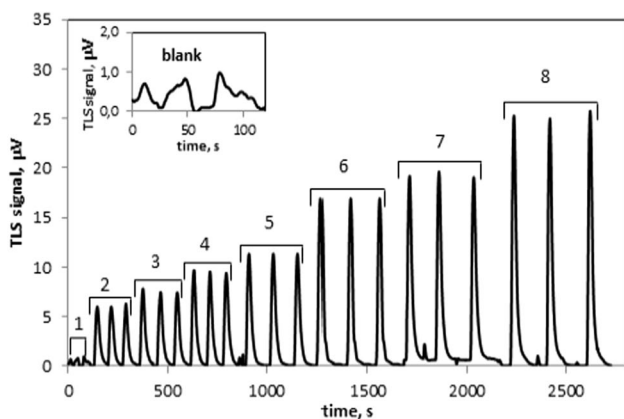


Figure 3 FIA signals for TLS detection of colloid silver corresponding to: 1—blank, 2—20 ng/mL, 3—40 ng/mL, 4—60 ng/mL, 5—80 ng/mL, 6—100 ng/mL, 7—120 ng/mL, and 8—160 ng/mL [36].

(see Fig. 3). A linear relationship between $\Delta I/I$ and A was established for low absorbances (sample concentrations < 0.6 mg/L), approximated via least-squares regression. This enabled curve parameter definition and limit of detection (LOD) calculation (refer to Table 1). The signals exhibited linear growth within the 0–80 ng/mL sample concentration range, with a standard deviation below 2.5% (refer to Fig. 4). LODs were calculated at a signal-to-noise ratio of 3 and for three excitation beam power levels of the 407 nm emission line, near the resonance band of produced silver colloids. The slopes correlated well with the linear TLS signal dependence on excitation power. Calculated LODs were: 1.2 μg/L for a laser power of 115 mW ($y = 720.7x$; $r^2 = 0.98$), 0.8 μg/L for a laser power of 155 mW ($y = 816.4x$; $r^2 = 0.99$), and 0.7 μg/L for a laser power of 195 mW ($y = 993.3x$; $r^2 = 0.98$). Additional parameters for LOD calculation are presented in Table 1. The findings suggest that elevating pump beam power could enhance LOD, particularly when increased excitation power does not raise the blank's standard deviation.

The achieved method's LODs significantly surpass the maximum contaminant levels (MCL) for silver in

Table 1 Parameters of calibration curves obtained for Ag⁰ NP detection by FIA-TLS for different powers P of ER

P (mW)	slope of the calibration curve (μV/mg/L)	Standard deviation of the blank (μV)	LOD (μg/L)
115	584.5	0.246	1.2
155	795.17	0.216	0.8
195	1068.5	0.241	0.7

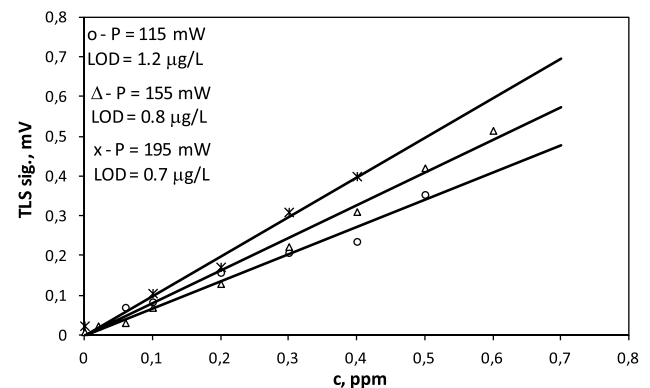


Figure 4 The calibration curves for three values of the output power of the Krypton laser used as the excitation.

water, which varies from 0.025 to 0.075 mg/L across countries and 0.2–0.5 mg/L for space missions, and notably outperform the LOD of 50 $\mu\text{g/L}$ achieved by spectrophotometry. The technique's applicability was tested for quantifying Ag^0 NP concentrations in water from Russian ISS drinking water supplies. Analysis was grounded on the calibration curve (refer to Fig. 4), with the TLS signal value determined for space water serving as the sample. For this, the reductant NaBH_4 was substituted with double-deionized water. The concentration of colloidal silver NPs was ascertained by substituting the reductant with double-deionized H_2O , yielding an Ag^0 NP amount of 0.094 ± 0.002 mg/L (Fig. 5).

Additionally, it was observed that various common ions found in water can notably disrupt the determination of Ag^0 and, consequently, its antibacterial efficacy, necessitating consideration when utilizing it as a disinfectant agent. This technique can be optimized using the IonPac Cryptand G1 column, enabling selective silver detection amidst foreign ions. The exceptionally high binding constant (K) of 2.2.2 cryptand for Ag^+ (109.6) surpasses all ions typically present in water supplies, which have been demonstrated to hinder Ag^0 NP detection. As a result of the strong complex formation with Ag^+ , the IonPac Cryptand G1 column selectively retains Ag^+ over other interfering ion complexes, enabling the discerning determination of Ag^0 NPs. This paves the way for the technique's application in selectively quantifying Ag^0 NPs in complex environmental samples, including natural waters.

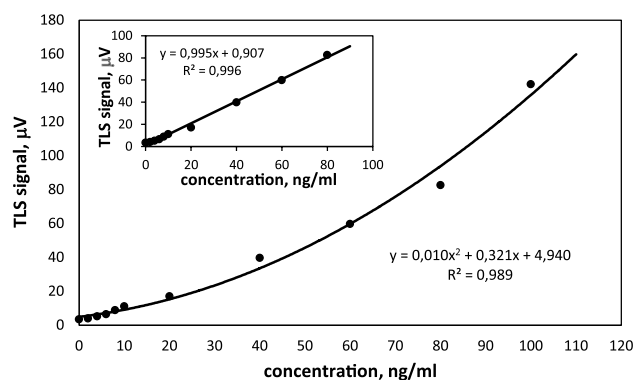


Figure 5 The TLS signal dependence on the concentration of Ag^0 NPs in batch mode measurements [36].

Photodegradation studies of modified multi-walled carbon nanotubes

The application of thermal lens spectrometry (TLS) for analyzing the degradation process of tartrazine as a model pollutant and multi-walled carbon nanotubes (MWCNTs) as photocatalysts under simulated sunlight irradiation was explored [44]. MWCNTs consist of nested long wall tubes with a diameter of up to 100 nm and length of up to 400 μm so that the aspect ratio lies typically between 50 and 4000, influencing their performance and application range. Their porous and high-surface area structure makes them valuable for environmental sensing, while their excellent thermal and electrical conductivity enhances insulating materials when added in small quantities, leading to various applications in electronics. Incorporating MWCNTs with Fe_3O_4 results in a high-strength magnetic material with catalytic applications in pollutant degradation [45]. The TLS experimental setup was employed in batch mode (BM) to investigate the electrochemical properties of MWCNTs-COOH/ Fe_3O_4 complex with NiO addition for photocatalytic tartrazine degradation. Surface area analysis via SEM revealed that Fe_3O_4 incorporation increased the surface area due to oxide deposits on nanotubes, whereas NiO incorporation reduced the surface area, possibly due to NiO entering the pores of MWCNT-COOH/ Fe_3O_4 (Fig. 6). TLS-BM experimental setup used in the study is displayed in Fig. 7. Each measurement in TLS-BM was replicated five times, and subsequently, the mean TLS signal value and its standard deviation were computed. To investigate the photodegradation of tartrazine, experiments were conducted under simulated sunlight irradiation. The lamp was positioned 20 cm from a 1 cm cell, illuminating the sample from the top for intervals of 1, 2, 5, 8, 12, and 20 min.

In order to evaluate the photocatalytic efficacy of the samples, a calibration curve ($y = 5.0765x + 1.3058$, $r^2 = 0.994$) was established within the concentration range of 0–10 mg L^{-1} for tartrazine. The achieved LOD was 10 $\mu\text{g L}^{-1}$, around 25 times lower compared to UV-vis spectrophotometry [44]. The utilization of MWCNT-COOH/ Fe_3O_4 nanocomposite coupled with simulated sunlight radiation led to an initial 20% enhancement in the rate of tartrazine degradation within the first 2 min of irradiation, decreasing to 10% after 5 min and halting its efficacy after 8 min, indicating incomplete pollutant decomposition with leftovers reaching 150% of the blank signal.

Figure 6 SEM images of **a** MWCNT, **b** MWCNT-COOH, **c** MWCNT-COOH/ Fe_3O_4 , and **d** MWCNT-COOH/ Fe_3O_4 /NiO [44].

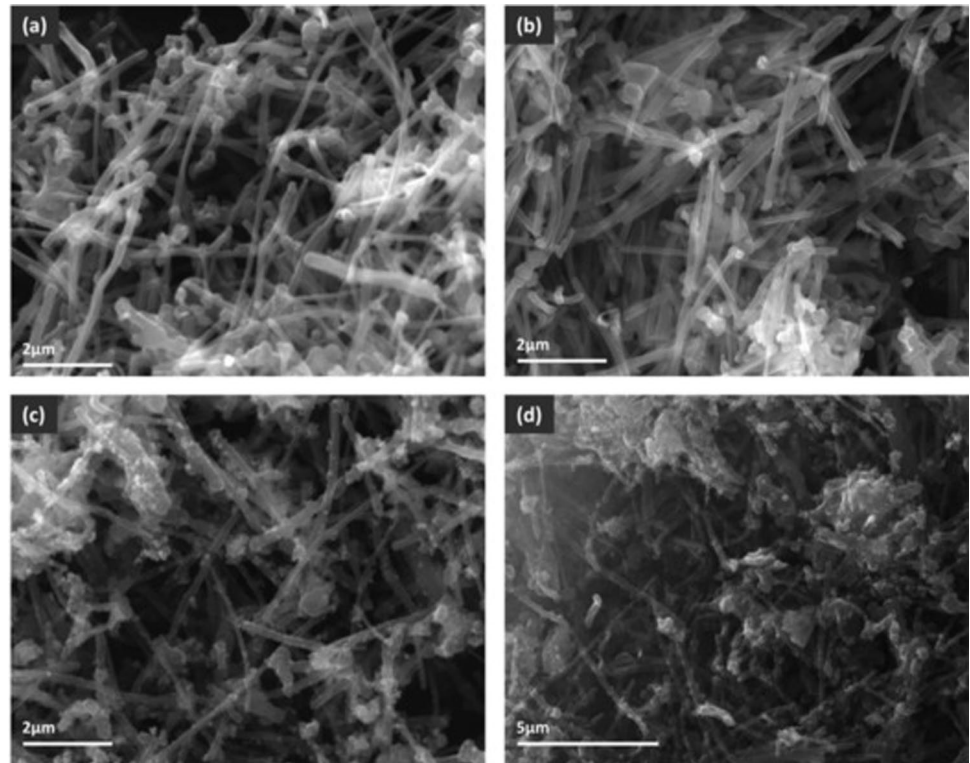
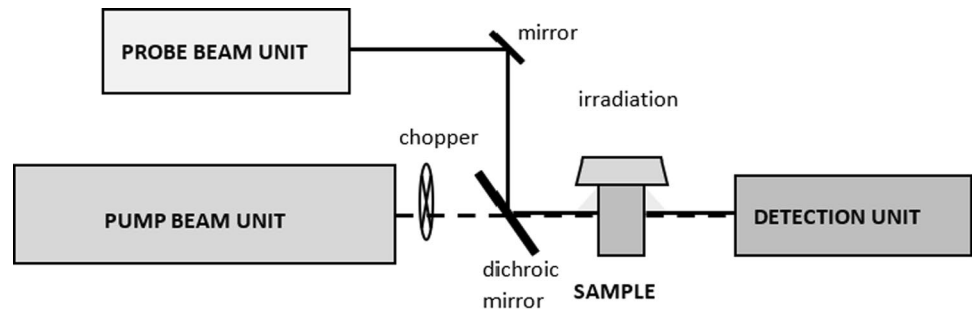


Figure 7 TLS-BM experimental setup with pump beam of 405 nm and probe beam of 632.8 nm.



In contrast, the implementation of MWCNT-COOH/ Fe_3O_4 /NiO nanocomposite as a photocatalyst, in conjunction with either 1 min of simulated sunlight irradiation or 5 min of MWCNT-Fe-Ni interaction without irradiation, yielded a TLS signal equivalent to the blank (Fig. 8). The enhanced photocatalytic efficacy of the nanocomposites in pollutant degradation can be attributed to the injection of photoinduced electrons from Fe_3O_4 to MWCNTs, reducing electron-hole recombination and promoting hole-electron separation rates at their interface [46, 47]. Additionally, the incorporation of NiO into MWCNT-COOH/ Fe_3O_4 diminishes material surface area while generating oxygen-rich functional groups that enhance the oxidation process and thereby

augment the photocatalytic activity compared to MWCNT-COOH/ Fe_3O_4 .

Photocatalytic reaction rate study

The ultra-sensitivity of the TL technique enables its application in the study of photocatalytic reaction rates. This section elucidates the TL technique's application in studying the photocatalytic reaction rates of the Cu- and Zr-modified TiO_2 photocatalyst. Titanium dioxide (TiO_2), particularly in nanoparticle (NP) form, emerges as a significant catalyst in water purification procedures owing to its enhanced reactivity over its bulk form, along with its non-toxic, biocompatible, and cost-effective attributes [48, 49].

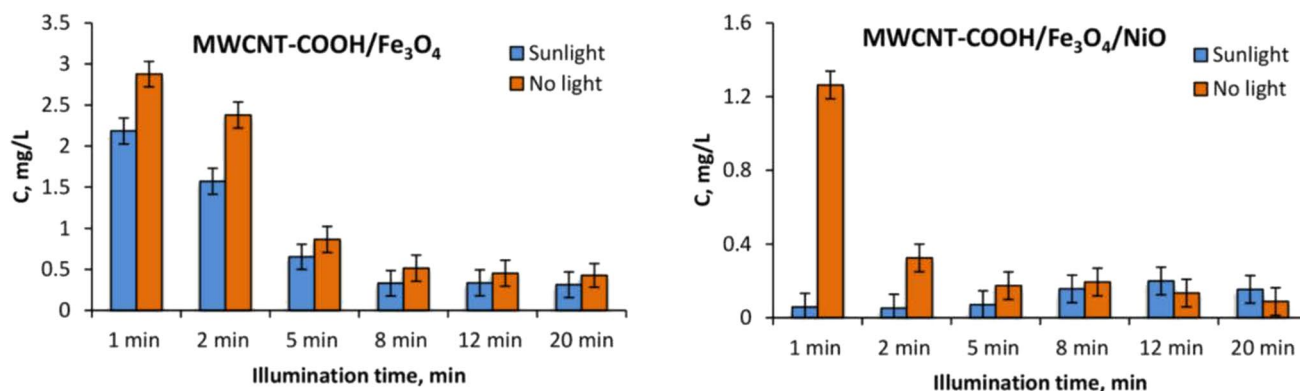


Figure 8 Decrease in tartrazine amount of leftovers concentration in the solution determined by TLS as a result of degradation by the use of synthesized nanocomposites and sunlight illumination [44].

In this work [50], Cu- and Zr-modified TiO_2 NPs were employed as photocatalysts for the degradation of reactive blue 19 (RB19) dye, serving as a test pollutant. The TLS technique was applied to monitor the photocatalytic reaction rate, utilizing the TLM-BM experimental setup shown in Fig. 7 with a pump laser at 532 nm and probe at 632.8 nm. Measurements were conducted under simulated irradiation from a 300-W UV lamp, emitting 13.6 W in the near-UV range (315–400 nm) and 3.0 W at shorter wavelengths (280–315 nm). The lamp was positioned vertically, 5 cm away from a 1 cm quartz cell, to irradiate the sample from the top. A 3 mL water solution containing 6 $\mu\text{g/L}$ of photocatalyst and initially 5 mg/L RB19 was illuminated for 50 min. After every 5-min irradiation interval, TLS measurements were conducted in the presence of unmodified TiO_2 photocatalyst and Cu/Zr-modified photocatalyst materials. To assess the photocatalyst efficiency, scrutiny of photocatalytic reaction rates is imperative, depicting the progress of the reaction characterized by first-order kinetics [51].

$$\ln(c/c_0) = -K_p t \quad (3)$$

where c_0 and c denote the concentrations of RB19 at the initiation and at time t of the photocatalytic reaction, respectively, while K_p represents the first-order rate constant of the photocatalytic reaction. The photocatalytic reaction rate is determined as the slope of the plot depicting the natural logarithm of (c/c_0) versus time t (Fig. 9).

The study reveals that the TiO_2 modified with Zr (1%), Cu (0.05%), and Zr (1%) Cu (0.05%) significantly amplifies photocatalytic reaction rates, accelerating the degradation of RB19, as shown in Table 2.

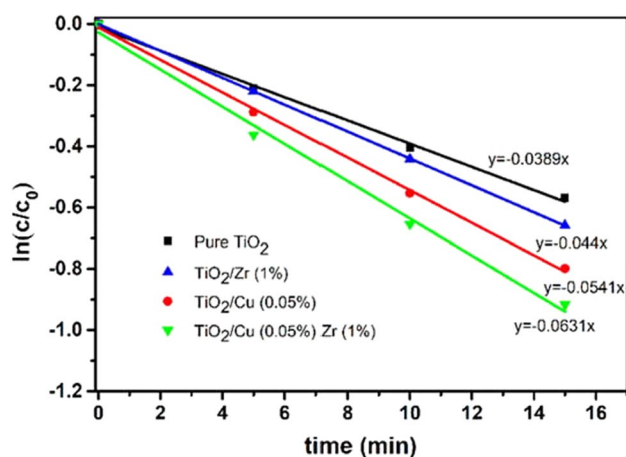


Figure 9 Decay profiles for first-order photocatalytic reactions during simulated solar light irradiation of RB19 aqueous solutions in the presence of unmodified TiO_2 and Cu- and/or Zr-modified TiO_2 materials [51].

Table 2 Photocatalytic reaction rate constants for unmodified TiO_2 and Cu- and/or Zr-modified TiO_2 materials [51]

Sample	$ K_p $ (min^{-1})
TiO_2	0.039 ± 0.001
TiO_2/Cu (0.05%)	0.054 ± 0.002
TiO_2/Zr (1%)	0.044 ± 0.001
TiO_2/Cu (0.05%) Zr (1%)	0.063 ± 0.002

These outcomes align with existing literature data [51–53] and are correlated with energy band cap values and carrier lifetimes of unmodified TiO_2 and Cu- and/or Zr-modified TiO_2 materials. Importantly,

Cu and/or Zr modification does not substantially alter crystallite particle size (around 25 nm) [51] but enhances the material surface area, facilitating pollutant adsorption and light absorption, thereby bolstering the pollutant degradation efficiency [50].

Single-beam TL study of the effect of allotropic transformation on the thermal diffusivity of soot nanofluid

The paper [54] focuses on enhancing the thermal diffusivity of nanofluids using soot, a mixture of carbon allotropes, as an example. According to existing literature [55, 56], soot is known to contain diverse carbon allotropes, including multi-walled (MW) and single-walled (SW) carbon nanotubes, graphene, fullerenes, amorphous carbon, and graphite. Gasoline soot annealed at different temperatures is used to prepare the nanofluid, and its morphological modifications are studied using field emission SEM (FESEM) and XRD. The FESEM image in Fig. 10 reveals that samples P30 (soot sample at room temperature) consist of soot particles with sizes ranging from 20 to 30 nm and

sample P400 (soot sample annealed at 400 °C) exhibits carbon nanotubes (CNTs) with diameters between 25 and 53 nm. Various techniques, including XRD and Raman spectroscopy, are employed to analyze signature peak intensities and structural changes in the soot samples with varying annealing temperatures. The thermal diffusivity of the nanofluid, containing the same solid volume fraction of soot, is investigated using the single-beam TL technique shown in Fig. 11.

Remarkably, the thermal diffusivity of the soot nanofluid shows oscillatory behavior, mirroring the changes observed in the XRD and Raman spectroscopic studies. The variation of percentage enhancement of thermal diffusivity of the NF containing soot annealed at different temperatures (P30–P400) is shown in Fig. 10c. The modifications in the carbon nanotubes (CNTs) and graphene layers significantly impact the thermal diffusivity, with an impressive enhancement of up to 95% for the soot annealed at 300 °C. However, the study also reveals the importance of maintaining the fluid temperature below 300 °C to avoid morphological and structural changes that could reduce the thermal diffusivity to 20%.

Figure 10 FESEM image of the sample **a** at room temperature -P30 **b** annealed at 400 °C -P400; **c** Variation of percentage enhancement of thermal diffusivity of the NF containing soot annealed at different temperatures [54].

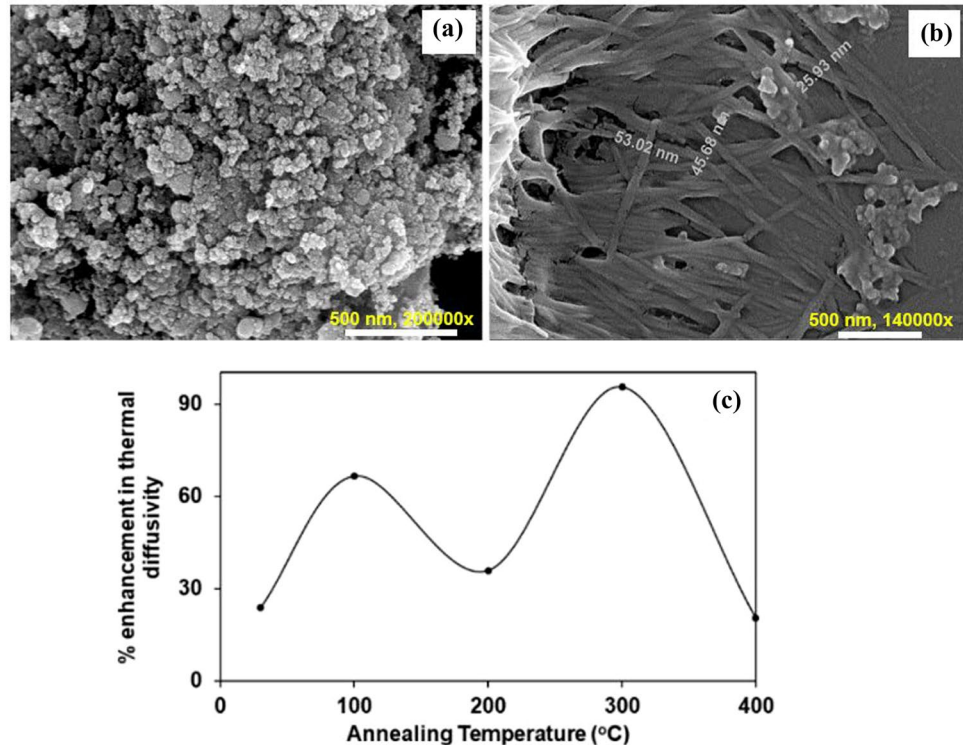
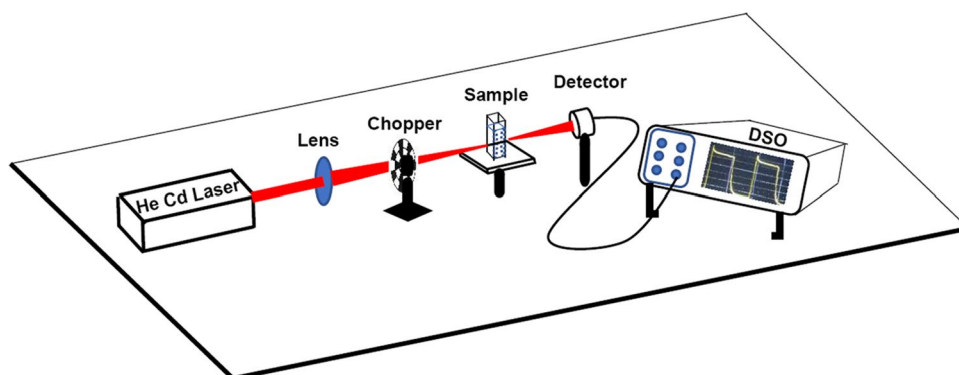


Figure 11 Schematic representation of single-beam thermal lens technique (SBTLT) [54].

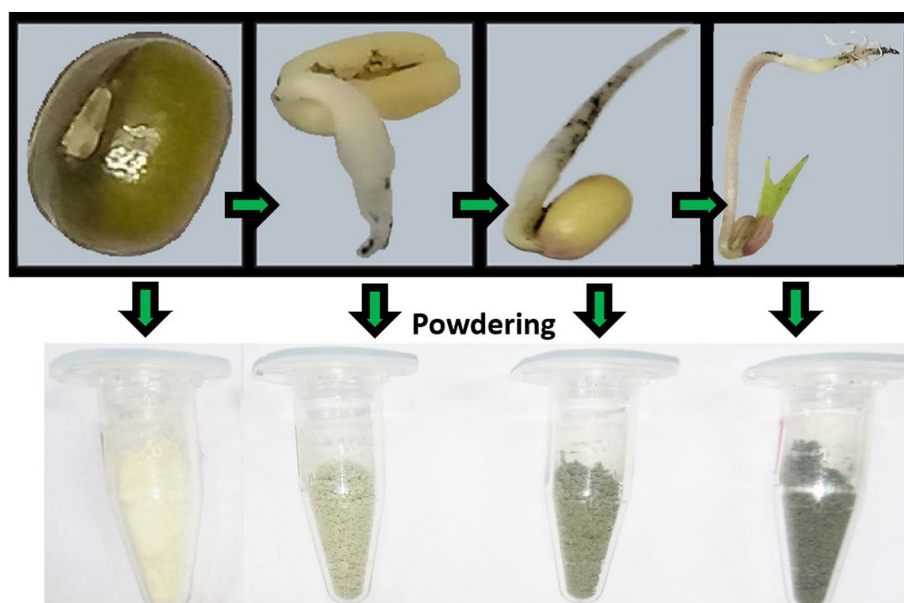


Nanobiophotonic application of single-beam TL technique: a study of tuning the thermal diffusivity of the seed matter

The work [57] explores the crucial role of thermal behavior in seed germination and growth using SBTLT detailed above (Fig. 11). Various carbon allotropes, including MWCNT, super graphene, diesel soot, and charcoal, are studied to understand their impact on the germination of *Vigna Radiata* (VR) seeds. Despite structural and morphological differences observed in the carbon allotropes through FESEM images, all of them enhance the seed's growth rate compared to the control set. The compositional variations in the seed matter modify its thermal behavior, as analyzed using SBTLT. A representative quantity of the seeds under examination undergoes a cleaning and grinding process and is subsequently transformed into a nanofluid

with 1 g of powder per liter of double-distilled water. Consequently, nanofluids derived from seeds germinating in water and diesel soot media are studied at four distinct germination stages (0 h, 24 h, 48 h, 72 h). The photographs of a representative seed and its seed matter are displayed in Fig. 12. The percentage variation of thermal diffusivity of the seed matter at different stages of germination in media with (D) and without (N) diesel soot is displayed in Fig. 13. The study reveals a reduction in the thermal diffusivity of seed matter in carbon allotropic medium (CAM), leading to energy trapping during biochemical reactions. This increased energy utilization contributes to the enhanced rate of biosynthesis during germination and seed growth. The seed matter's compositional changes are further analyzed through UV-Vis-NIR, FTIR, and PL spectroscopic techniques, providing insights into the formation of chlorophyll molecules

Figure 12 Representative photographs of seed and its seed matter at different stages of germination [57].



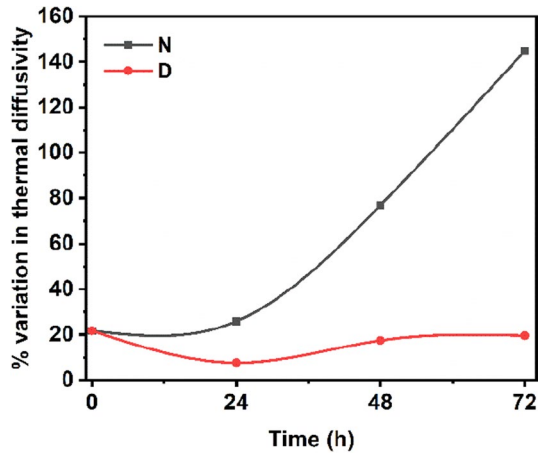


Figure 13 Percentage variation of thermal diffusivity of the seed matter at different stages of germination in media with (D) and without (N) diesel soot [57].

and nucleotides during germination in the carbon allotropic medium (CAM). This research offers a mechanism of CAM-assisted germination for producing healthy plants with high yields in a shorter time, thereby addressing food security concerns in a world facing challenges of population growth and carbon emission-induced pollution.

Understanding molecular dynamics in heat transfer nanofluids from TL signal through nonlinear time series analysis

The current study [7] explores the molecular and particle dynamics occurring in MWCNT nanofluids prepared at three different concentrations (C1-0.02 g/l, C2-0.04 g/l, and C3-0.08 g/l), in base fluids [water (MW), ethylene glycol (ME), and acetone (MA)] of varying viscosity. This investigation uses nonlinear time series and fractal analyses to analyze the thermal lens (TL) signal. The research holds significance in designing energy-efficient and high-performance thermal systems through nanofluids with tailored thermal diffusivity and sample entropy, achieved by selecting suitable base fluids and nanoparticles. To validate the characteristics of the MWCNTs, their morphological, structural, and optical properties are confirmed using FESEM, XRD, Raman, and UV-visible spectroscopic analyses. The results from the thermal diffusivity study reveal that particle dynamics play a significant role in low viscous media due to reduced viscous drag force, leading to greater freedom of movement and

faster heat transfer rates, consequently increasing thermal diffusivity. Conversely, thermal diffusivity decreases in highly viscous base fluids, but increasing the concentration of MWCNTs enhances thermal diffusivity regardless of the base fluid. These findings align well with the Sankar–Swapna model, which considers thermal diffusivity's dependence on the medium's viscosity. During the heat transfer process, complex particle and molecular dynamics are analyzed through phase portraits, sample entropy, fractal dimension, and Hurst exponent analyses. The complexity in MWCNT nanofluids (C1, C2, and C3) within low viscous base fluids is evident from the phase portraits, sample entropy, and fractal dimension analyses. The representative excerpts of TL signal, phase portrait, and sample entropy variations from the literature [7] are shown in Fig. 14.

Additionally, the complexity of particle dynamics in nanofluids exhibits an inverse relationship with the base fluid's viscosity. The increasing anti-persistence nature in samples MA (MWCNT nanofluid in acetone) and MW (MWCNT nanofluid in water) further confirms nanofluid's rising complexity. As a result, the nonlinear time series analysis of the TL signal presents a novel methodology for understanding the particle/molecular dynamics-driven heat transfer property of nanofluids, offering insights into tuning thermal diffusivity and sample entropy. Knowledge of these parameters is essential in thermal engineering to enhance the efficiency of thermal systems.

Complex network analysis of TL signal of nanofluids

The study [58] reveals how soot facilitates energy movement within leaves by analyzing time-resolved TL signals' graph properties. Different concentrations of soot particles, containing various carbon allotropes, are applied to *Lablab purpureus* (L.) sweet leaves. After ten days, leaves are collected, and extracts are made at concentrations of 0.20 (P1), 0.60 (P2), 1.25 (P3), 2.50 (P4), 4.00 (P5), and 5.00 (P6) g/l. UV-Vis spectroscopy is conducted to comprehend the impact of carbon nanoparticles (CNPs) on leaf pigment absorption. The SBTL technique is then applied to nanofluid samples, and their varying TL signals are analyzed graph-theoretically. The representative complex networks constructed from the TL signal of samples P0 and P3 are shown in Fig. 15. The constructed network showcases a complex structure with unconnected nodes, edges,

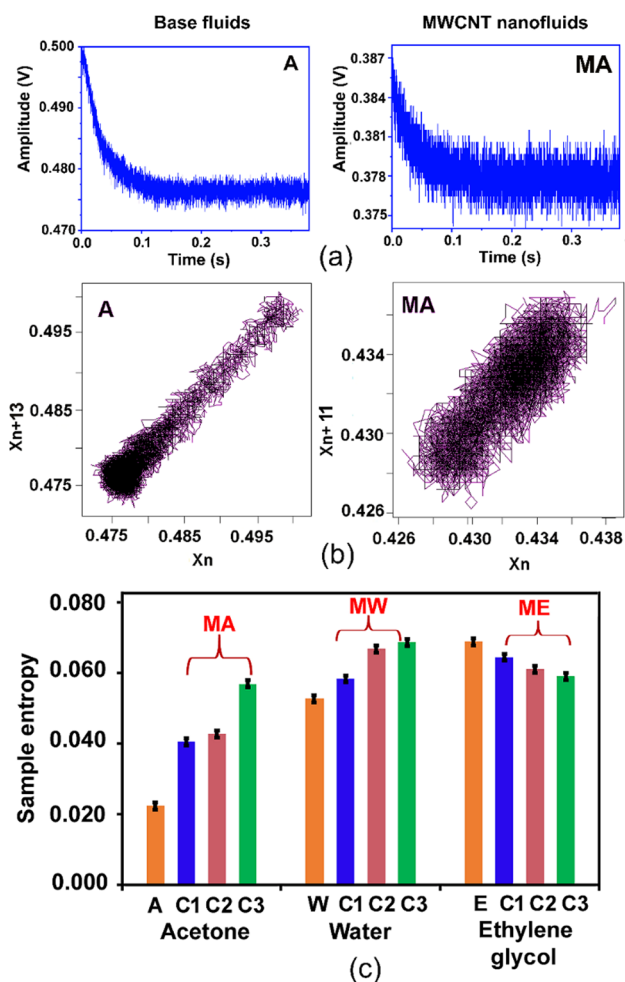
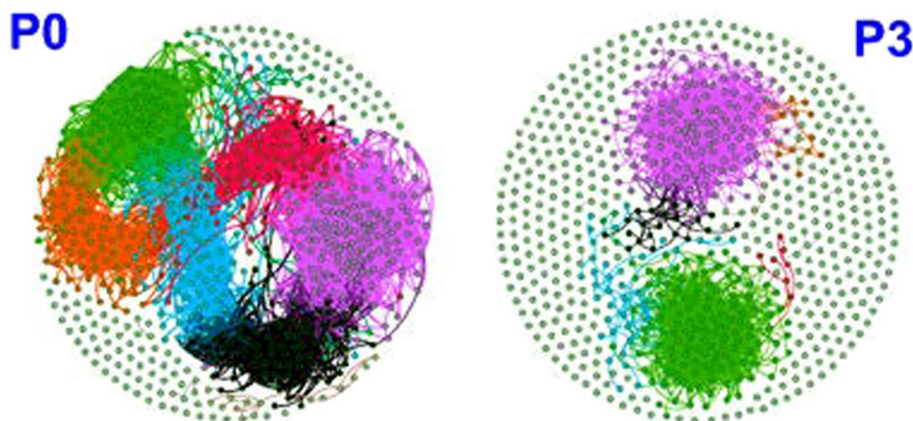


Figure 14 A representative **a** TL signal and **b** phase portrait of base fluid acetone and MWCNT nanofluids with acetone; **c** variation of sample entropy for the samples MA, MW, ME—MWCNT nanofluid in acetone, water, and ethylene glycol, respectively [7].

Figure 15 Representative complex networks constructed from the TL signal of samples P0 and P3 [58].



and clusters. Graph complexity variations are related to optical absorption and thermal energy flow in nanofluids. Topological graph features (E-edges, D-diameter, ND-network density, NC-number of components, C-closeness centrality) align with absorbance changes; higher CNP concentrations show increased absorption. Sample P3 with 1.25 g/l CNP has maximum absorbance and enthalpy, reflected by more uncorrelated nodes in the graph. Comparing this with acetone, NC increase relates to system enthalpy rise. Graph features in two regions (R1, R2) show CNPs first absorb and re-emit energy, then initiate the intra-pigmental transfer, favoring photosynthesis, but excessive CNPs do not significantly enhance transfer due to saturated enthalpy. Sample P3 with maximum enthalpy has the least E, D, ND, and C values, suggesting an optimum CNP concentration of 1.25 g/l for efficient intra-pigmental energy transfer and enhanced photosynthesis.

Photoacoustic spectroscopy and applications

In PAS, the absorption of ER and its further non-radiative release causes the thermoelastic expansion of the illuminated sample volume and, consequently, the generation of acoustic waves in the surrounding fluid [59, 60]. The most often used setup configuration for characterizing a two-layered system is an open photoacoustic cell (OPC) [61, 62] that ensures greater signal strength than other PAS experimental setup configurations.

Theoretical description

The investigated sample is a two-layered structure in the form of a thin film deposited on a bulk substrate. The film is a transparent dielectric layer that is uniformly

enlightened by ER and absorbs its whole radiation, whereas the substrate is a semiconductor material (Fig. 16) [63]. In the analysis, it is also assumed that the whole structure is of cylindrical symmetry and a total thickness of $l = l_1 + l_2$ (l_1, l_2 are the sample and support thicknesses, respectively) that is much smaller than the structure radius R_s as shown in Fig. 16.

The PA signal obtained from the sample presented in Fig. 16 includes the thermal diffusion (TD) effect, which is dominant in PA signals at a lower modulation frequency of ER, as well as both thermoelastic (TE) and plasma elastic (PE) effect that have the significant influence on PA signal at a higher modulation frequency of ER [62, 64, 65], and is described by:

$$\delta p_{total}(f) = \delta p_{TD}(f) + \delta p_{TE}(f) + \delta p_{PE}(f) \quad (4)$$

where $\delta p_{TD}(f)$, $\delta p_{TE}(f)$, and $\delta p_{PE}(f)$ are the thermal diffusion, thermoelastic, and plasma elastic PA signal components, respectively, expressed by [62, 64, 65]:

$$\delta p_{TD}(f) = \frac{p_0 \gamma_g}{\sigma_g l_c} \frac{T_2(l, f)}{T_0} \quad (5)$$

$$\delta p_c(f) = \frac{\gamma p_0}{V_0} \int_0^R 2\pi r U_z(r, z) dr \quad (6)$$

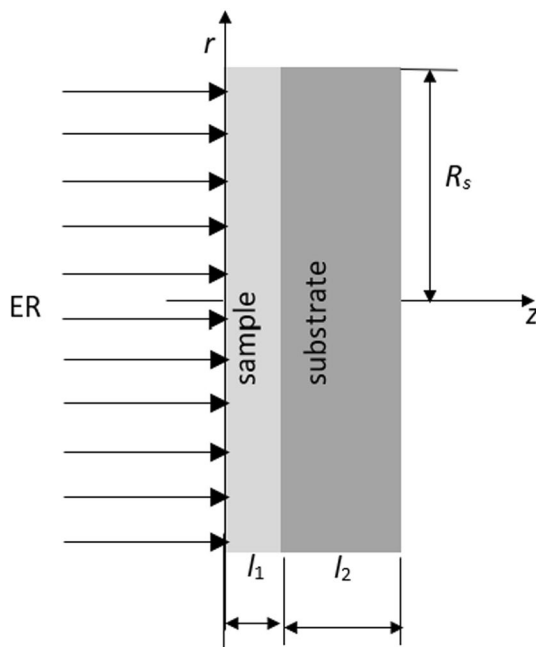


Figure 16 The configuration of the experimental setup.

where $c = TE, PE$ in case of thermoelastic (TE) and plasma elastic (PE), respectively, γ is the adiabatic constant, p_0 and T_0 are the equilibrium pressure and temperature of the air in microphone, $\sigma_g = (1 + i)\mu g$, μg is the thermal diffusion length in the air; l_c is the distance between sample and microphone membrane, $T_2(l, f)$ is the periodic temperature variation at the substrate rear (non-illuminated) surface, V_0 is the OPC volume, and $U_z(r, z)$ is the sample displacement along the z -axes.

Thus, the total PA signal defined as a pressure wave generated by the periodic sample heating as a result of its irradiation by ER can be written as [65]:

$$\delta p_{total}(f) = A(f) \exp[i\varphi(f)] \quad (7)$$

Here, $A(f)$ is the PA signal amplitude and $\varphi(f)$ the PA signal phase, whereas i the complex unit.

Thermal and elastic characterization of nanostructured Fe₂O₃ polymorphs

The examined samples were α - and ϵ -Fe₂O₃ polymorphs, and these polymorphs with deposited ultra-thin layers of TiO₂ that tailor their properties for light-activated applications [66]. The morphology of the Fe₂O₃ polymorphs was studied by using FESEM. It was found that α -Fe₂O₃ is characterized by particles of pyramidal shape (lateral size and length = 600 and 1000 nm, respectively), as well as globular particles (lateral size and length = 300 and 600 nm, respectively), that are randomly distributed, creating a topography of disordered agglomeration (Fig. 17). ϵ -Fe₂O₃ present a more uniform morphology having the form of rod-like structures perpendicular to the substrate surface (Fig. 17) with the mean nanorods lateral size and length of 80–350 nm, respectively. The rod-like structures also showed a cylindrical trunk (≈ 300 nm) and a sharper tip (≈ 50 nm).

In the analysis, the sample was considered to be a two-layered structure. The thin film of Fe₂O₃ material (1st layer with a thickness of 800 nm and 450 nm for α -Fe₂O₃ and ϵ -phase, respectively) was deposited on a Si substrate (2nd layer with a thickness of 736 μ m). The ultra-thin TiO₂ layer (thickness ~ 10 nm) deposited on a Fe₂O₃ film was considered a constitutive part of the Fe₂O₃ layer with the same effective thermal parameter values.

The PAS measurements were performed using the experimental setup presented in Fig. 18 [62]. As an ER, a laser diode with a power of 15 mW and 660 nm

Figure 17 **a, c** Plane-view and **b, d** cross-sectional FESEM micrographs for **a, b** α -Fe₂O₃ and **c, d** ϵ -Fe₂O₃.

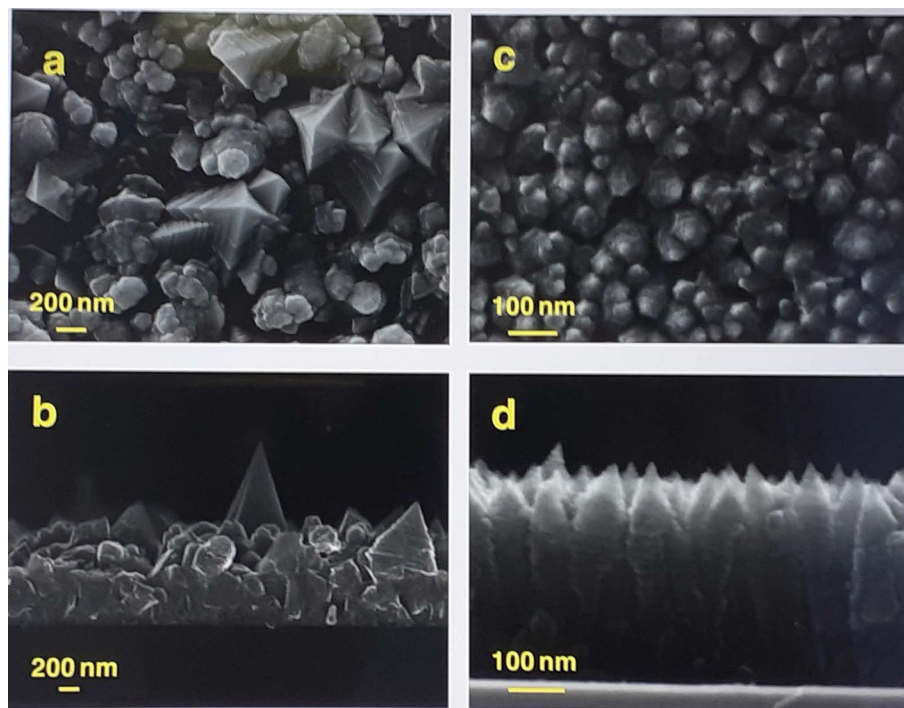
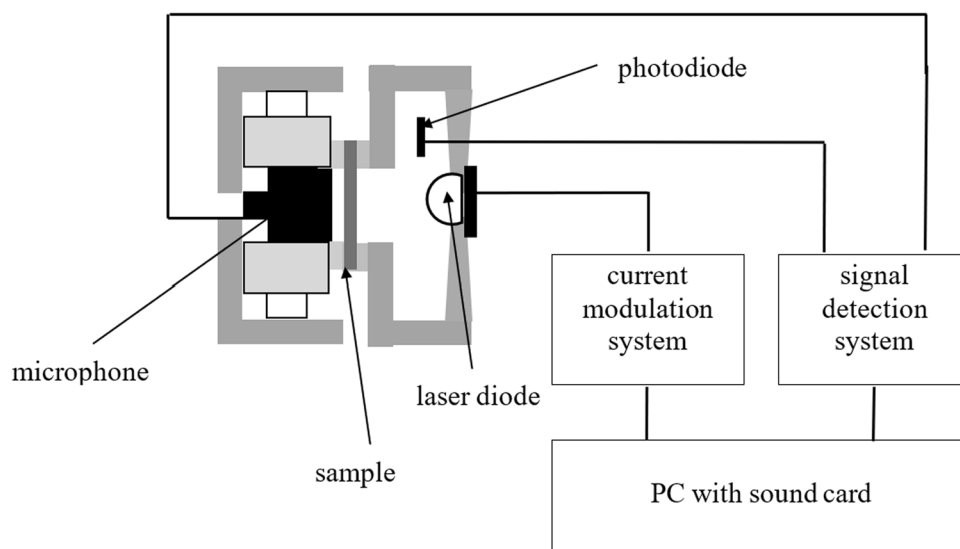


Figure 18 Scheme of the PAS experimental setup used in the study.



was used and modulated in the frequency range of 20 Hz–20 kHz by a homemade current modulator. ER light intensity was monitored by a photodiode. The examined sample was placed in a homemade PA chamber, and its front surface was uniformly illuminated by ER to satisfy the condition of the 1D configuration of the setup. A battery-powered electret microphone monitored the changes in the pressure in the PA chamber. The PC audio controller is used to emulate lock-in amplifier signal processing

to extract the amplitudes and phases of the acoustic signal.

The PA signal amplitudes and phases collected for different Fe₂O₃ polymorphs without (α -Fe₂O₃, β -Fe₂O₃) and with ultra-thin Ti-based layer (α -Fe₂O₃-TiO₂, β -Fe₂O₃-TiO₂) together with the fitted theoretical dependencies are presented in Fig. 19. The $S_{\text{exp}(f)}$ represents the measured PA signal ($A_{S_{\text{exp}(f)}}$ -amplitude, $\varphi_{S_{\text{exp}(f)}}$ -phase), whereas the $\delta p_{\text{total}(f)}$ ($A_{\delta p_{\text{total}(f)}}$ -amplitude, $\varphi_{\delta p_{\text{total}(f)}}$ -phase) is the 'true'

Figure 19 The amplitude and phase of PA signal collected from **a** α -Fe₂O₃; **b** α -Fe₂O₃-TiO₂; **c** ϵ -Fe₂O₃; and **d** ϵ -Fe₂O₃-TiO₂, deposited on Si support, together with the fitted theoretical dependences as a function of modulation frequencies of ER [63].

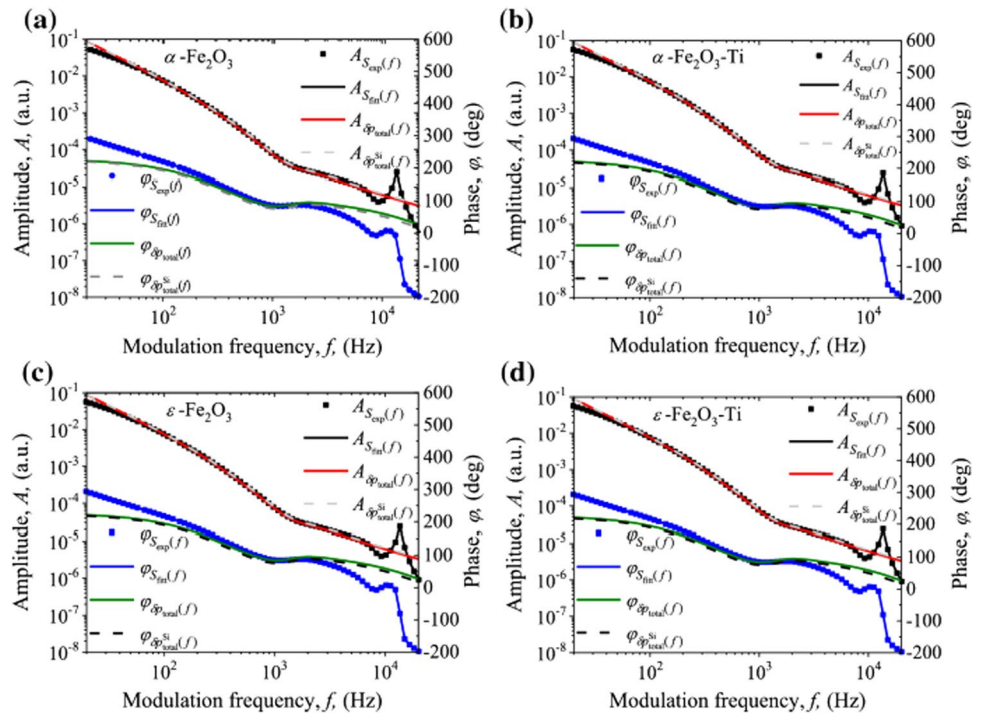


Table 3 The values of determined thermal and elastic properties of different Fe₂O₃ polymorphs [63]

Sample	$D_{T1} (\times 10^{-7} \text{ m}^2/\text{s})$	$k_1 (\text{W/mK})$	$\alpha_{T1} (\times 10^{-6} \text{ K}^{-1})$
Si/ α -Fe ₂ O ₃	100 ± 5	12.5 ± 0.3	12 ± 3
Si/ α -Fe ₂ O ₃ -TiO ₂	$90 \pm 5^*$	$11.5 \pm 0.3^*$	$11 \pm 4^*$
Si/ ϵ -Fe ₂ O ₃	120 ± 8	14.4 ± 0.4	23 ± 2
Si/ ϵ -Fe ₂ O ₃ -TiO ₂	$110 \pm 9^*$	$13.7 \pm 0.4^*$	$22 \pm 3^*$

*Effective values for the entire thin-film layer (polymorph + ultrathin TiO₂)

two-layer signal obtained after performing the signal correction procedure [67, 68], $S_{\text{fit}}(f)$ ($A_{S_{\text{fit}}(f)}$ -amplitude, $\phi_{S_{\text{fit}}(f)}$ -phase) are the fitting curves, and $\delta p_{\text{total}}^{\text{Si}}(f)$ is the PA signal generated by Si substrate ($A_{\delta p_{\text{total}}^{\text{Si}}(f)}$ -amplitude, $\phi_{\delta p_{\text{total}}^{\text{Si}}(f)}$ -phase). The obtained values of the determined parameters can be found in Table 3 [63].

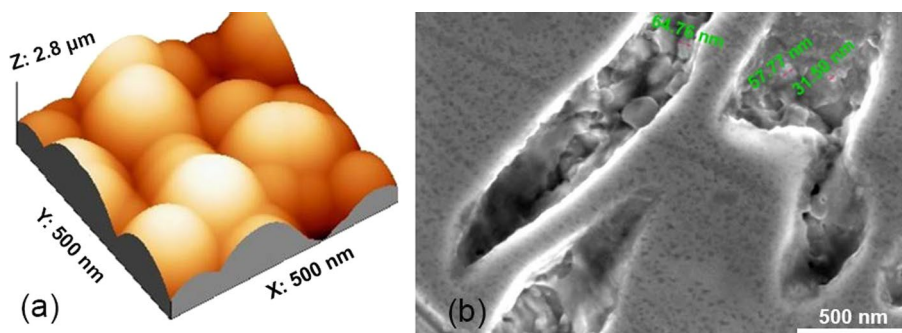
It can be seen that α -Fe₂O₃ has lower values of thermal and elastic parameters compared to ϵ -Fe₂O₃ as a consequence of different polymorphs morphology. ϵ -Fe₂O₃ has a more compact structure with fewer interfaces than α -Fe₂O₃ [69]. Furthermore, the surface of ϵ -Fe₂O₃ is flatter than that of α -Fe₂O₃ [69]. After TiO₂

deposition on the Fe₂O₃, both the thermal and elastic properties of α - and ϵ -Fe₂O₃ polymorphs change due to the whole sample morphology change.

Optical and thermal characterization of metal mirrors

The PA technique finds applications in the optical and thermal characterization of metal mirrors, possessing the advantage of consistently generating high-quality, distortion-free images over an extended period. In one of the studies [70], we elucidated the potential of the PA technique in determining the reflection coefficient and thermal diffusivity of a specific metal mirror, namely the Aranmula mirror. This particular mirror, characterized by its high reflection coefficient, holds significant importance in optical instrumentation applications. To gain insights into the mirror's surface, we assessed its reflectivity, which is influenced by the root mean square (rms) roughness. Employing atomic force microscopy (AFM) analysis (Fig. 20), we quantified the rms roughness, and the results indicated that the metal mirror exhibited a surface roughness of 146 nm, contributing to its overall reflective behavior. Further analyses were conducted to study the mirror's structural characteristics and composition. Using FESEM, we explored the surface smoothness

Figure 20 a AFM image and b FESEM image of the inner view of the metal mirror [70].



and identified the presence of particles within the mirror. The XRD analysis revealed that the metal mirror was an alloy of copper (Cu) and tin (Sn), with an average crystallite size of 33 nm, indicating its complex composition and nanostructure.

In this study, an Argon ion laser with a wavelength of 488 nm was employed. The metal mirror was placed in the photoacoustic cell, and an intensity-modulated laser beam irradiated it while varying the chopping frequency. The energy absorbed by it was converted into mechanical energy, resulting in pressure variations and an acoustic signal in the photoacoustic cell. The amplitude of the acoustic signal (s) was measured using a lock-in amplifier, which allowed for in-phase signal detection and effectively eliminated noise signals, thereby significantly enhancing the signal-to-noise ratio. By investigating the dependence on the thermal diffusion length on chopping frequency (f) and the sample thickness (l_s), the transition point from a thermally thin to a thermally thick regime can be noted as a change of slope in the log (amplitude) versus log (f) plot at the characteristic frequency (f_c) (Fig. 21). The thermal diffusivity (α) is determined using $\alpha = l_s^2 \cdot f_c$. The α of the metal mirror was calculated from $f_c = 68.79$ Hz and $l_s = 1.24$ mm as 1.058 ± 0.001 cm²/s.

The reflection coefficient holds significant importance in characterizing mirrors, especially for metal mirrors used in reflecting telescopes. In this research, the laser-induced PA technique was employed to find the reflection coefficient of the mirror, with a carbon black sample used as a reference. By noting the photoacoustic signal amplitudes (S_m and S_C) for the Aranmula mirror and carbon black, respectively, at a given chopping frequency and laser power, the ratio of mirror-to-carbon black signal amplitudes was calculated as [70]

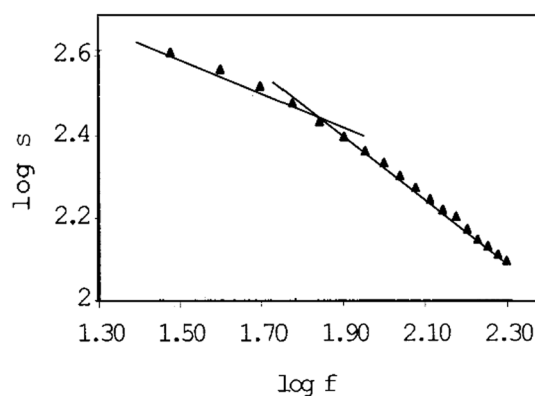


Figure 21 log (signal amplitude, s) versus log (chopping frequency, f) plot of the sample

$$\frac{S_m}{S_C} = \frac{IA_m}{IA_C} = \frac{A_m}{A_C} \quad (8)$$

where ' I ' represents the incident beam intensity, and A_c and A_m denote the absorption coefficients for carbon black and the mirror, respectively. Since A_c for carbon black is equal to 1, the reflection coefficient (R) can be directly determined by analyzing the variation of signal amplitude with modulating frequency, as $R = 1 - A_m$. The reflection coefficient of the metal mirror was obtained as 0.92.

Investigation of optical properties of the ZnO nanoparticles grown on porous surface of diatomite

Diatoms are photosynthetic microorganisms that are enclosed within hydrated amorphous silica cell walls. Such microorganisms live in aquatic environments. Since they exhibit nanoporous structures with high surface area and biocompatibility, they find application in drug delivery systems [71–73]. Many efforts were made to improve diatoms properties by their

surface or structure modification with inorganic (e.g., TiO₂, MgO, Au) and/or organic materials (e.g., polyaniline, organosilane) [74]. One of the most investigated materials to be combined with diatoms is ZnO, which presents large exciton binding energy and wide optical energy band gap and thus becomes a promising material in different optoelectronic or photocatalytic devices [75, 76].

The PA spectroscopy in a non-resonant configuration of the cell [77] was applied to investigate ZnO nanoparticles grown on the surface of diatomite. The source of EB was a Xe lamp modulated by a mechanical chopper and equipped with the monochromator, enabling collecting the PA signal within the wavelength range of 300–700 nm by a microphone with a low-noise preamplifier as displayed in Fig. 22. The collected PA signal of examined samples was normalized to the reference signal that was a 1-mm-thick optically opaque carbon glass sample.

In the case of ZnO nanoparticles grown on the surface of diatomite, it is seen from Fig. 23 that a strong absorption occurs in the 300–450 nm range, indicating that such materials are effective in light absorption enhancement and, thus, of high potential as materials used for efficient light capturing [71] without the need of further material treatment. Such behavior is not observed for pure diatom samples. This results from strong light absorption by the dispersed ZnO NPs for $\lambda < 450$ nm that is not present for $\lambda > 450$ nm, for which ZnO becomes transparent, and any difference in PA signal behavior cannot be observed for both types of samples. Since the PA signal carries information about the sample's optical properties, the values of absorption β_a and scattering β_s coefficients can be extracted from PA measurements according to the procedure described in the literature [71]. Enhancement of both absorption and scattering coefficients of ZnO nanoparticles grown on the surface of diatomite found in

Figure 22 Scheme of the experimental setup used in the study.

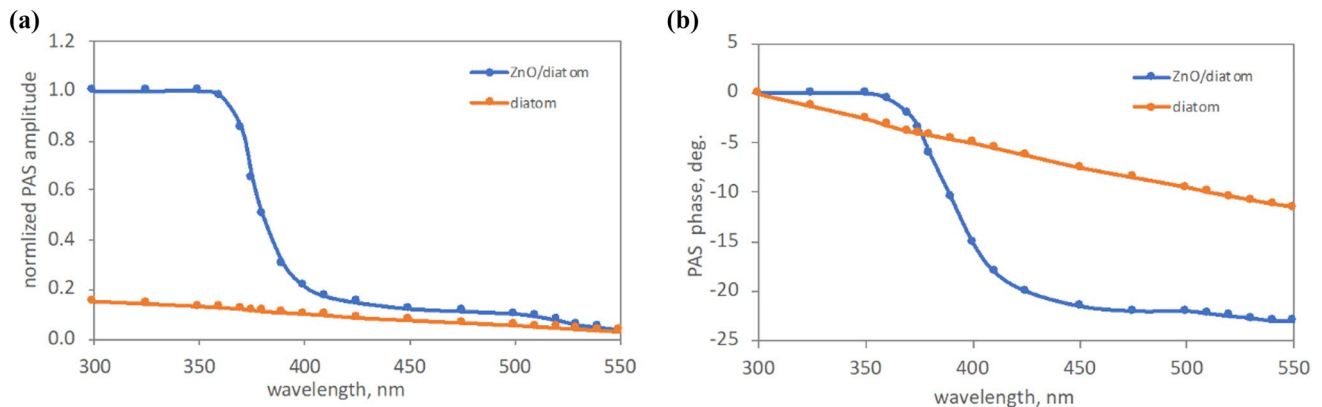
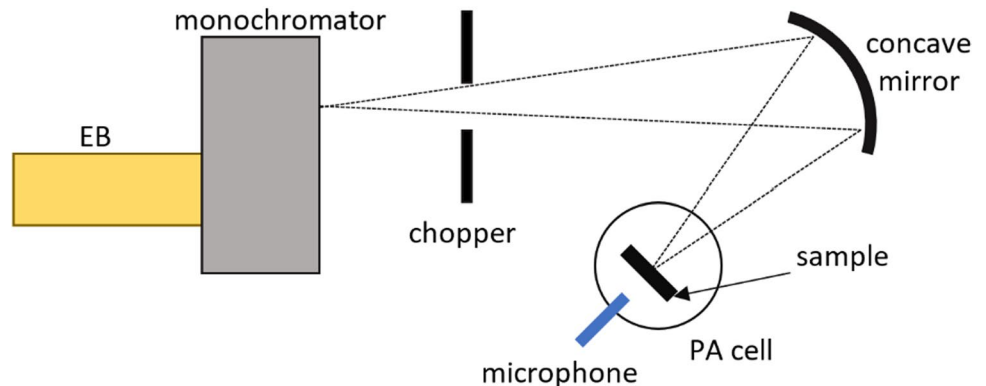


Figure 23 Normalized PAS amplitude (a), and phase (b) obtained for ZnO nanoparticles grown on the surface of diatomite at 25 Hz modulation frequency of EB.

the wavelength range of 300–450 nm can be observed that does not occur for pure diatom samples (Fig. 24).

Analysis of nanoparticle degradation promoted by a polymer coating

The PA technique was applied to monitor and control the kinetic degradation process of silicon NPs (Si NPs) with surface-engineered properties in colloidal solution to examine their potential for application as efficient delivery systems in cancer curation [78]. Colloidal Si NPs were polymer (polyallylamine PAA) coated and suspended in distilled water. Such modified Si NPs are positively charged due to the presence of PAA on their surface, thus attracting hydroxyl (OH^-) ions, which increases the pH around the Si NP surface and further enhances its degradation process.

The PA measurements were performed by the use of homemade experimental setup for real-time detection of degradation of Si NPs in colloid solution. The EB was the second harmonic of a nanosecond Nd:YAG laser at the wavelength of 532 nm that coincides with the detected NP's absorption spectra, optimizing

the photoacoustic conversion efficiency. ER was collimated and split by a plate beam splitter. The split reflected beam was used to monitor ER intensity by a PIN Si photodetector. The split transmitted beam was expanded by a 50 mm focal length concave lens and directed through a cuvette containing colloidal solution of Si NPs. The expanded EB ensures the illumination of the major part of the cuvette to avoid errors caused by NP sedimentation and prevent Si NPs from photodamaging. The generated PA signal was collected by an acoustic transducer stuck to the cuvette wall by ultrasonic gel. Both cuvette and transducer were placed in a thermally controlled FLASH 300 module equipped with optical windows for transmitting EB. The reflected EB from the beam splitter as well as the PA signal was collected by an oscilloscope triggered by a laser pulse (Fig. 25).

The PA signal was found to depend linearly on the Si NPs concentration in water (Fig. 26a) with the LOD of 0.2 $\mu\text{g}/\text{mL}$. Furthermore, Si NPs are found to be stable in water for the whole observation period (1 day), whereas, for Si NPs in PBS (Phosphate buffer saline), a drop to 20% level with the half-life of $t_{1/2} = 400$ min

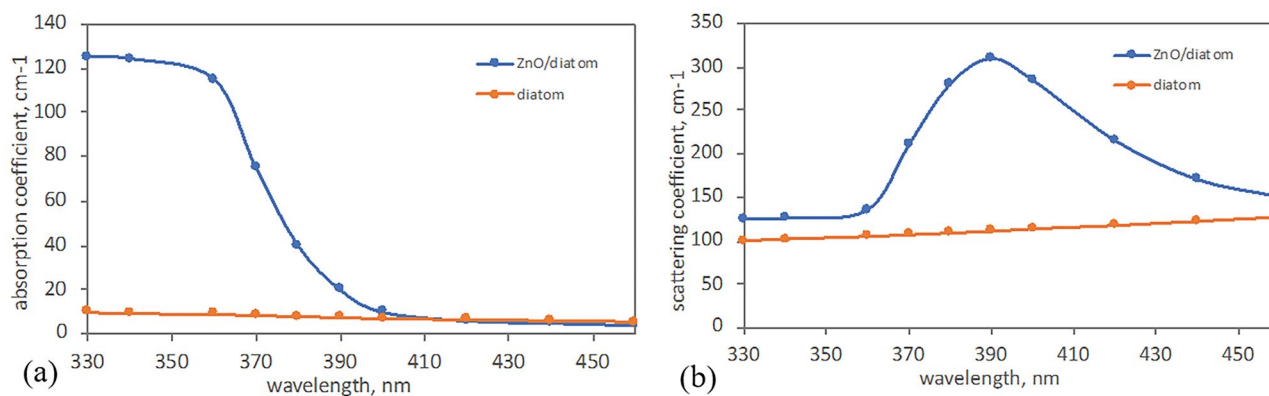
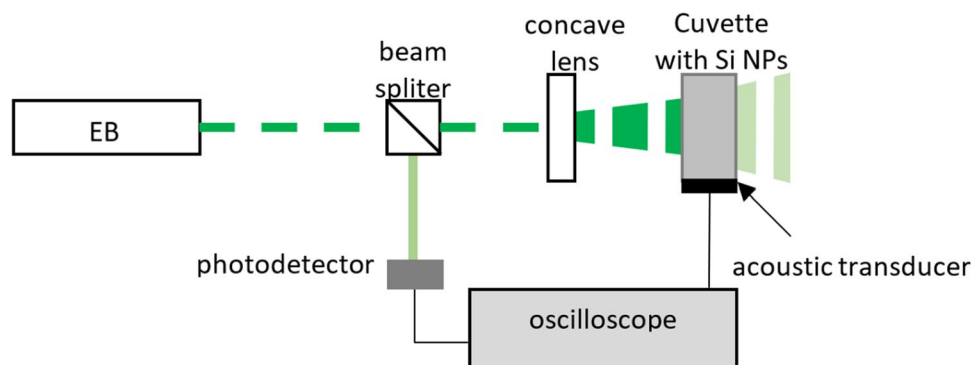


Figure 24 Spectrum of the absorption (a) and scattering (b) coefficient obtained from the PA measurements.

Figure 25 Scheme of the experimental setup used in the study.



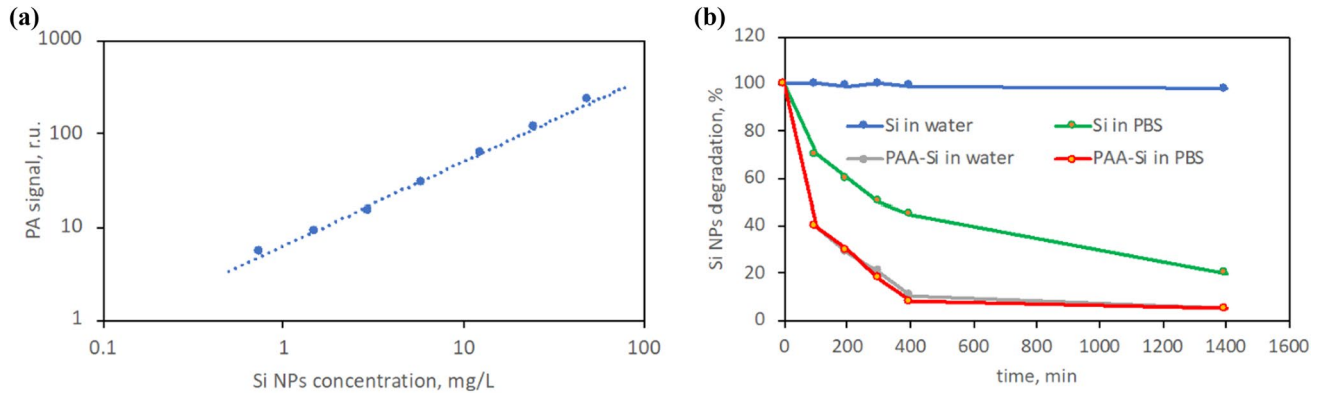


Figure 26 **a** Calibration for Si NPs determination in distilled water by PA technique and **b** kinetics of degradation of Si NPs/PAA-Si NPs in water/PBS solution at 37 °C.

(Fig. 26b) is seen. In the case of PAS-Si NPs, almost the same degradation kinetic is observed with the half-life of $t_{1/2} = 104$ min (Fig. 26b) for both water and PBS solution. Thus, the PA technique can be applied for direct observation of the Si NPs fate in highly scattering fluids (e.g., biological samples), making it a promising technique when designing and screening biodegradable materials for in vivo applications.

Investigation of thermal transport in porous silicon nanostructures and nanowires

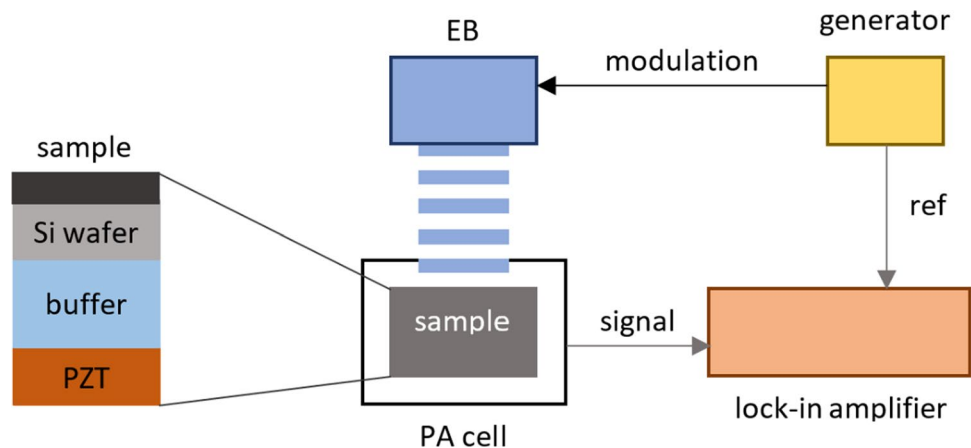
Integrating and miniaturizing electronic systems for different applications requires the implementation of NMs, which enable tuning the structure and thermal properties crucial for designing integrated functional devices. In this work, silicon-based nanomaterials (Si NMs) as porous silicon nanostructures (P Si NSs) and silicon nanowires (Si NWs) are examined by the use of PA spectrometry in a piezoelectric configuration [79].

Porous Si NSs are characterized by relatively low thermal conductivity and, thus, found application as efficient thermal isolators. In contrast, Si NWs are materials with strongly anisotropic thermal conductivity values, making them useful in applications requiring efficient guidance of heat flux.

The main drawback of the PA technique is the working frequency range introduced by the microphone used to detect the photoinduced acoustic signal, which can be overcome by using configurations with piezoelectric detection. Figure 27 presents the scheme of the experimental setup used in the study.

The light-emitting diode of 407 nm output wavelength was used as EB, whose intensity was square-wave modulated in a frequency range from 10 Hz to 20 kHz. The illuminated sample has a multilayered structure, as shown in Fig. 27. Its thermoelastic deformation caused by light absorption of EB is detected by a piezoelectric transducer, which was in tight acoustic contact with the sample through a

Figure 27 Scheme of PA experimental setup used for piezoelectric detection.



buffer layer. The PA signal's amplitude and phase were collected by the use of a lock-in amplifier (Fig. 27). To extract the values of thermal conductivities of P Si NSs and Si NWs, a proper theoretical model was developed [79] further used in the fitting procedure of theoretical dependences to the experimental data. The examined samples were P Si NSs with different porosities and Si NWs with different lengths, whereas the fitted parameter was the material's thermal conductivity. The results obtained in the study are given in Table 4.

It was found that the Si NSs have much smaller values of thermal conductivities than the bulk Si materials that is 150 W/m K [80]. Furthermore, P Si NSs have lower thermal conductivity compared to Si NWs (Table 4), a consequence of the morphological features of P Si NSs matrix. Finally, the thermal conductivity of the Si NWs decreases with the increase in their lengths as the result of Si NWs in-depth structural inhomogeneity.

Table 4 Values of thermal conductivities determined for different Si NSs [79]

			Thermal conductivity (W/m K)
P Si NSs (50 μm thick)	Porosity (%)	45	2.3 ± 0.2
		55	1.8 ± 0.2
		65	1.4 ± 0.1
Si NWs (porosity = 50–55%)	Length (μm)	20	7.3 ± 0.4
		35	6.2 ± 0.3
		50	5.6 ± 0.3

Characterization of core/shell (Ag/CdSe) nanostructure

The combination of Ag/CdSe metal/semiconductor NS enables the adjustment of its absorption band to suit particular applications in light energy conversion systems [81]. It is performed by controlling the core size and shell thickness to obtain the proper choice of core-to-shell ratio. The PA technique was applied to determine the optical and thermal properties of Ag/CdSe NS in a powder form. The PA measurements were performed in the wavelength range between 400 and 700 nm at a modulation frequency of 16 Hz using the experimental setup shown in Fig. 27. The PA spectra were light intensity normalized using carbon black. An example of PA spectra for a sample of Ag core and CdSe shell is presented in Fig. 28.

The character of PA spectra is the result of the influence of the surface plasmon absorption bands of the Ag core and the band gap of CdSe shell (Fig. 28a). Determining the 2nd derivative of the PA signal, the peak absorption wavelength of the whole material is obtained (Fig. 28b). Furthermore, performing the fitting of polynomial function to the 2nd derivative of experimental data, the size of the CdSe shell is found [82]. The obtained values were in the range of 2.57–4.77 nm. The thermal diffusivities of the Ag/CdSe NSs were found by performing PA measurements in frequency scan mode of Ag/CdSe NSs compressed into a disk of 0.5 mm thickness and applying the equation [82]

$$D = f_c L^2 \quad (9)$$

where $L = 0.5$ mm and is the thickness of the compressed Ag/CdSe NSs, whereas f_c is the characteristic

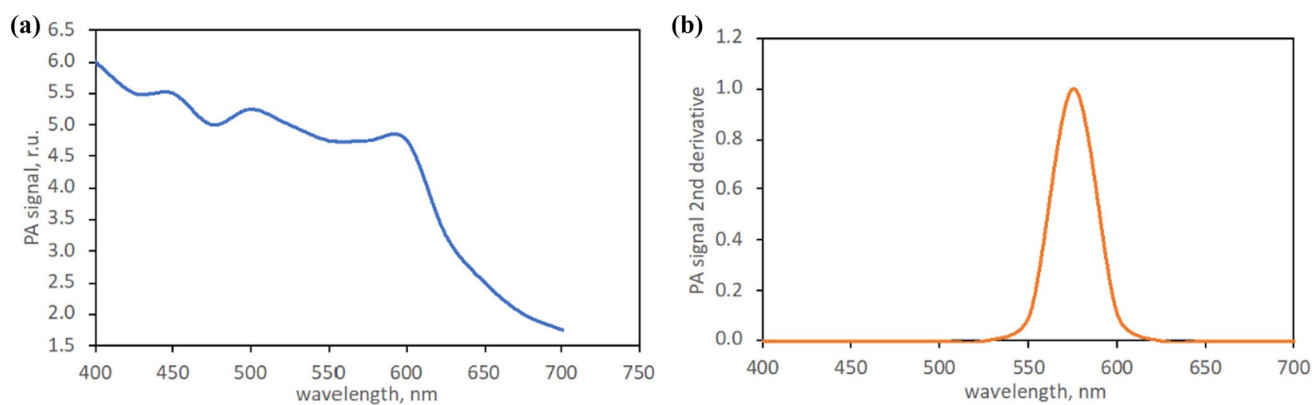


Figure 28 **a** The PA spectra and **b** related 2nd derivative of the 14–15 nm Ag core and 3.52-nm-thick CdSe shell.

frequency [82]. The obtained values of thermal diffusivities of Ag/CdSe NSs are in the range of 0.098 cm²/s and 0.14 cm²/s, which is an order of magnitude higher than the bulk value of pure CdSe (0.014 cm²/s) and thus makes the whole Ag/CdSe material more efficient for application as solar conversion devices.

Determination of thermal properties of nanofluids containing Ag nanowire

NPs are widely used as additives to fluids to create suspensions (nanofluid NF) with improved heat transfer properties that are controllable by proper choice of NP's material, sizes, shapes, and concentrations [83]. Thus, it can be used in many industrial applications, such as medicine, electronics, transportation, chemical, and food engineering. In this work [84], the properties of Ag NWs are examined to determine their potential as additives in the preparation of nanofluids.

The PA technique was used in open cell configuration (Fig. 29). The NF sample is placed on the aluminum foil with known thermal effusivity. An electret microphone detects the acoustic waves generated by EB modulated by a mechanical chopper at frequency *f*. The PA signal is collected by a lock-in amplifier and normalized using the PA signal collected for the air sample. In the first step, the PA cell was calibrated by measuring the PA signal for water as a sample. The thermal effusivity of the sample is then calculated by the use of equation [84]:

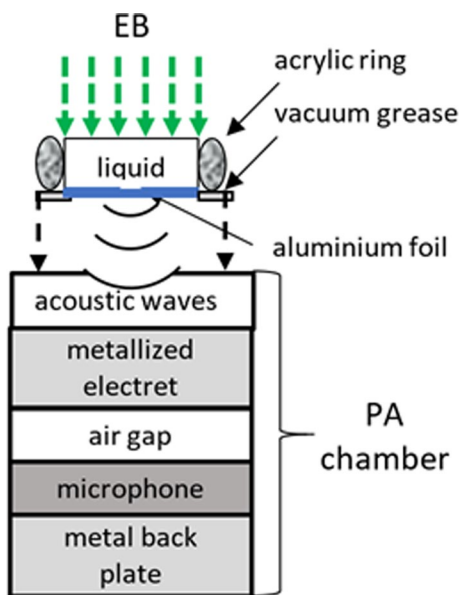


Figure 29 Scheme of the open photoacoustic cell.

$$e_s = \frac{I_0 c_0 \rho_0}{I_R} \sqrt{2\pi f} \tag{10}$$

where ρ_0 , c_0 , l_0 are the density (2.7–3.0 g cm), specific heat (0.9 Jg⁻¹ °C⁻¹), and thickness of the aluminum foil (16 μm), respectively, whereas I_R is the slope of the normalized PA signal as a function of the square root of *f* (Fig. 30) [83].

The NF's thermal effusivities were obtained for fluids with different concentrations of Ag NWs. Based on their values, the thermal properties of Ag NWs were found using relations describing the thermal diffusivity [83]:

$$D_s = \frac{k_s}{\rho_s c_s} \tag{11}$$

and effusivity [84]:

$$e_s = \sqrt{k_s \rho_s c_s} \tag{12}$$

where k_s , $\rho_s c_s$ are the thermal conductivity and volumetric heat capacity of NF. The results are presented in Table 5 [83].

The enhancement of thermal properties was calculated as [83]:

$$E = \frac{p_s - p_{\text{water}}}{p_{\text{water}}} 100\% \tag{13}$$

where p_i is the thermal parameter of fluid (i = water for water, i = *s* for NF). The thermal conductivity of water was taken as 0.613 Wm⁻¹ K⁻¹ [85], thermal diffusivity as 14.0 × 10⁻⁸ m² s⁻¹ [86], and thermal effusivity as 1570 W s^{1/2}/m² K [87]. It was found that the thermal parameter's enhancement was in the range

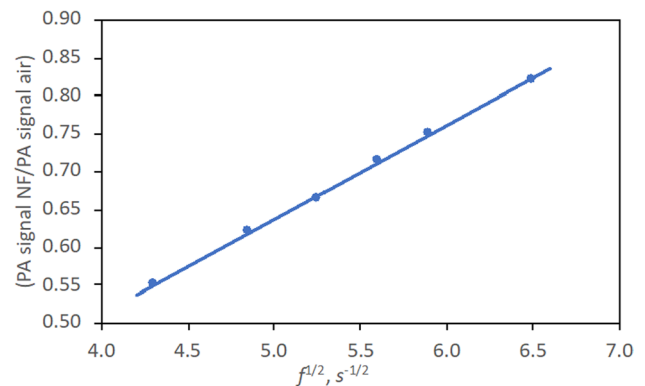


Figure 30 Normalized PA signal as a function of $f^{1/2}$ for NF containing Ag NWs with a concentration of 7 × 10⁻⁴ Vol%.

Table 5 Thermal diffusivity, effusivity, and thermal conductivity of the examined NFs [83]

Ag NWs/water (vol%)	3.5×10^{-6}	4.7×10^{-6}	7.0×10^{-6}	1.36×10^{-4}	1.74×10^{-4}
$D_s \times 10^{-8}$ (m ² s ⁻¹)	14.00 ± 0.18	15.11 ± 0.20	16.04 ± 0.17	16.58 ± 0.16	17.75 ± 0.24
e_s Ws ^{1/2} m ⁻² K ⁻¹	1663 ± 32	1687 ± 26	1688 ± 41	1694 ± 125	1716 ± 52
k_s Wm ⁻¹ K ⁻¹	0.622 ± 0.013	0.656 ± 0.011	0.676 ± 0.017	0.690 ± 0.051	0.723 ± 0.023

of 40–20.8 for volumetric fraction between 3.5×10^{-6} and 1.74×10^{-4} vol%. Thus, such NFs can be successfully applied as cooling liquids for highly efficient electronic devices, heat exchangers, or solar energy systems.

Advantages, limitations, and future challenges

Thermal lens spectrometry

The goal of the review is to present the advantages and limitations of the TLS technique and to indicate those applications in which TLS can potentially be a more powerful analytical method than conventional absorption techniques. Over time, TLS found a significant number of applications for NMs characterization and, thus, experienced rapid developments in theoretical descriptions and optical schemes [88–91]. Nevertheless, it has not yet become a routine chemical and biological analysis technique because of the lack of low-cost, portable, and easy-to-operate tunable light sources that could provide both ER and PB, which are crucial elements of the TLS experimental setups [88, 89]. Furthermore, the TL signal is measured as the far-field change in PB spot size by sensing its power at the PB axis; thus, the precise alignment of the experimental setup is required in combination with providing the optimum position of ER's and PB's waists with respect to the position of the sample cell. The path length in the examined sample must be much smaller than the confocal distance of ER and PB. All of this makes the whole system difficult for non-professional users to use, requiring the support of qualified people in the field [31, 92]. Another drawback of the TLS instrument is its limited tunability, which consequently limits its versatility since the lasers used as ER provide output radiation at only a few different wavelengths. In cases of low-volume samples, transferring the detection system to micro/nanospace involves substituting the TLS with thermal lens microscopy (TLM). This shift necessitates a combination of more theoretical analysis and experimental measurements [34, 93–98] to investigate the TLM signal behavior regarding experimental setup

parameters, aiming to enhance measurement sensitivity lost due to a path length approximately 100 times shorter than in conventional TLS.

Another advantage of TLS is the sensitivity enhancement compared to conventional transmission signal measurements using absorption spectrophotometry that is determined by the type of used solvents and condition of the experimental setup [99] and can be improved by applying solvents with appropriate properties that are those with high refractive index gradient (dn/dT) and low density (ρ), thermal conductivity (k), and heat capacity (c_p) according to Eq. (14) for detection performed using cw-TLS and Eq. (15) in case of pulsed-TLS [99]:

$$E_{\text{cw}} = \frac{P}{\lambda_p k} \frac{dn}{dT} \quad (14)$$

$$E_{\text{pl}} = \frac{4Q}{3\lambda_p c_p \omega_{\text{exc}}^2} \frac{dn}{dT} \quad (15)$$

Here, l_p is the PB wavelength, whereas ω_{exc} is the min ER radius focused in the place of the sample cell. From the above equations (Eqs. 14 and 15) arises that the measurement sensitivity of TLS can also be improved by increasing the ER either power P (cw-TLS) or irradiance Q (pulsed-TLS), which in turn increases the convective noise of the measurements, introduce nonlinear absorption effects as well as lead to saturation of the TLS signal [32, 100–102]. Convection noise is produced by convective movements of the liquid sample in the area of TL, which induces changes in material temperature that consequently lead to distortion of the sample refractive index gradient. Consequently, after PB interaction with TL, the PB intensity profile is distorted, degrading the TLS signal. This effect increases with the superior thermo-optical properties of the sample and the elevated background absorption we encounter. All of these can significantly increase the technique's LOD, thus limiting its sensitivity. The problem of background absorption can be eliminated in the simplest way by using differential TLS [103, 104] where the signal is measured as an

optical difference between the background signal and the signal from the analyzed sample.

Generally, the noise in TLS experiments can be eliminated or significantly reduced by applying the lock-in amplifier to detect the PB intensity changes induced by the photothermal effect [103] since, in such a case, only the signal component of the ER modulation frequency is measured. Furthermore, the TLS signal-to-noise ratio (SNR) can be improved by increasing the value of the integration time of the used lock-in amplifier, which should be adjusted regarding the stability of the signal. As a result of TLS signal saturation [103], the amount of ER radiation absorbed by the sample and later converted into heat does not further increase with the increase in the ER power/irradiance, which negatively impacts the sensitivity of the TLS method.

The TLS measurements are also strongly affected by the composition of the sample matrix [104–106]. The influence of electrolytes addition to the sample on the measurement sensitivity can be either positive or negative. The improved sensitivity was observed in the case of water sample solution, whereas the decrease in sensitivity was found for organic liquids used for sample preparation. This effect is caused by the changes in the thermo-optical properties of the whole solvent introduced by the addition of electrolytes.

Nevertheless, all the drawbacks mentioned above can be overcome or at least limited to specific TLS technique applications, making it very competitive compared to traditional transmission measurements. Future challenges in this field include the affords of automatization of the TLS instrument, which would simplify the procedure of its alignment and optimization and make the whole instrument more user-friendly. Another important step in TLS development would be exchanging the ER laser source to an incoherent light source, making the instrument broadband. It can be concluded that the development of TLS is at the level that makes it applicable as a tool for routine characterization of NMs.

Photoacoustic spectroscopy

This paper also gives an overview of PA experimental schemes currently used for NM characterization in a nondestructive way, enabling simultaneous determination of many NM properties. Such multiparametric sensitivity of the PA signal makes the whole analysis rather complicated and time-consuming, requiring a

deep understanding of all mechanisms contributing to PA signal generation. Thus, it is necessary to develop a specific configuration of the PA experimental setup providing the maximum sensitivity for determination of the desired NM parameter and minimizing as much as possible the influence of all the others on the measured PA signal [107–109].

The main advantages of the PA technique include the contactless and nondestructive way of sample characterization since the method is based on the detection of pressure waves induced by absorbed ER that eliminate thermal contact resistance and parasitic heat losses on the measured signal. The sensitivity of the PA technique is not limited by the absorption coefficient values, the sample's transmittance or the presence of scattering particles as it is in conventional transmission/absorption spectroscopy [110]. PA signal is generated only by the fraction of absorbed ER radiation that is released then back in the form of heat. Thus, scattering does not influence the thermal state of the material under investigation. This reduces the procedure of sample preparation significantly since processes such as filtering does not need to be performed.

Furthermore, the PA technique ensures a wide dynamic range of measurements that enables performing the measurements of NMs in which absorption coefficients are spread over several orders of magnitude from weak absorbing samples that require setting with short path lengths to highly absorbing or opaque samples without the necessity of their dilution. The structural properties of the NMs determine the PA signal since they determine the heat conduction within it and its exchange with the surroundings; thus, it may be extracted from the measurements by developing a proper relation with the generated PA signal. PA measurements provide not only the ability of a wide range of NM's parameters determination but also the possibility of solid sample depth-profiling by changing the modulation frequency of ER, which enables the PA signal collection from the bulk of the sample to its sub-surface layers as well as performing both in situ analysis and PA imaging of samples that present high contrast [111].

The disadvantages of the PA technique may be related to the complex process of extracting the desired NM properties from the measured PA signal, which must often be supported by a complicated theoretical analysis that needs to be performed for the specific system configuration [63, 112]. The selection of the proper experimental configurations for

NM characterization is determined by the samples' size as well as the predicted range of the parameters of our interest, which means that we must know the order of NM's parameter value that we are looking for [113]. Also, PA cells must be calibrated using material with known properties to eliminate cell effects on the determined values of examined NM, which makes the analysis longer and more complicated. Some difficulties with quantitative analysis can also be met, especially when applying the PA technique for PA imaging [114], since the measured signal depends on the local light intensity reaching the area of NM of our interest that, in turn, is influenced by the optical properties of material between the targeted volume of NM and the surface of it which ER illuminates. This problem can be solved by implementing an appropriate theoretical description of the PA signal generation in such a situation. The PA imaging was further developed for microscale, creating PA microscopy (PAM). In the PAM technique, the ER radiation is tightly focused on the material surface, which provides a high spatial resolution of the PA image that can be collected from depths up to 100 mm [115, 116] by moving the ER source over the surface of the sample and detecting the resulted PA signal. Nowadays, the biggest challenge of PAM that needs to be solved is monitoring the moving features, e.g., living objects [117–119].

Conclusions

Delving into the multifaceted examination of nanomaterial properties gives insights into the unique characteristics that differentiate them from conventional materials. This thorough comprehension forms the foundation for using nanomaterials across various domains such as catalysis, electronics, energy storage, and many other applications. This capability allows for the customization of their properties to suit specific requirements, thereby maximizing their effectiveness. Photothermal techniques, such as thermal lens spectrometry and photoacoustic spectrometry, offer advantages of elevated sensitivity and broad applicability across diverse sample types. Developing new measurement techniques, especially those based on the photothermal effect, is essential for precise NM characterization and property determination, paving the way for their continued exploration and application in contemporary technologies.

The objective of this review is to provide a concise overview of the utilization of prominent photothermal techniques, such as thermal lens spectrometry (TLS) and photoacoustic spectrometry (PAS), in the characterization of NMs. The review underscores the versatile applications of TLS in diverse fields, showcasing its efficacy in trace detection, photodegradation studies, photocatalytic reaction rate analysis, and nanobiophotonic investigations. The trace detection of silver nanoparticles in drinking and surface water samples utilized TLS coupled with FIA, eliminating the need for stabilizers that could interfere with metal surfaces. Moreover, TLS was employed to analyze the photodegradation process of tartrazine and MWCNTs under simulated sunlight, demonstrating its potential in environmental studies. The technique was further applied to assess the photocatalytic reaction rates of Cu- and Zr-modified TiO₂ nanoparticles in degrading RB19 dye, showcasing its relevance in catalysis studies. The exploration of soot nanofluids aimed at enhancing thermal diffusivity featured a single-beam TLS study, highlighting its role in optimizing nanofluid properties. The nanobiophotonic application of single-beam TLS revealed insights into seed germination and growth, offering a mechanism for accelerated and healthy plant development. The nonlinear time series and fractal analyses of TL signals on heat transfer nanofluids with MWCNTs shed light on the molecular and particle dynamics at different concentrations in base fluids of varying viscosity. The study on complex network analysis of TL signals in nanofluids, soot incorporated chlorophyll pigments, reveals insights into the optimal concentration for efficient intra-pigmental energy transfer and enhanced photosynthesis. These findings highlight the significance of TLS in unravelling the intricacies of nanomaterial behavior and its broad applicability across scientific disciplines.

Different nanostructured materials have been investigated using the photoacoustic (PA) technique, throwing light on their thermal and optical properties. The study delved into the thermal and elastic characterization of Fe₂O₃ polymorphs, revealing distinctive differences between α -Fe₂O₃ and ϵ -Fe₂O₃, with ϵ -Fe₂O₃ displaying lower thermal and elastic parameters due to its more compact structure. The addition of a TiO₂ layer further modified the properties of both polymorphs. Investigating metal mirrors demonstrated the PA technique's efficacy in determining the reflection coefficient and thermal

diffusivity of the Aranmula mirror, which is crucial for optical instrumentation applications. ZnO nanoparticles grown on diatomite surfaces exhibited strong absorption in the 300–450 nm range, understood from the PA spectrum, emphasizing their effectiveness in light absorption enhancement. The PA technique also played a pivotal role in monitoring and controlling the degradation kinetics of silicon nanoparticles (Si NPs) in colloidal solutions. The study on silicon-based nanomaterials, including porous silicon nanostructures (P Si NSs) and silicon nanowires (Si NWs), revealed their distinct thermal conductivities and highlighted the technique's capability to address working frequency limitations. Additionally, PA was employed to characterize core/shell (Ag/CdSe) nanostructures and determine thermal properties in nanofluids containing Ag nanowires.

The versatile thermal lens and photoacoustic spectroscopy applications across many nanomaterial studies underscore their invaluable roles in unveiling nanostructured materials' intricate thermal, optical, and structural characteristics, paving the way for tailored advancements in diverse scientific and technological domains.

Acknowledgements

The authors Mohanachandran Nair Sindhu Swapna and Dorota Korte acknowledge the financial support from Slovenian Research Agency (project J7-2602 and P2-0393).

Data availability

Not applicable.

Declarations

Conflict of interest All authors declare that they have no conflict of interest.

Human participants and/or animals rights Not applicable.

Informed consent Not applicable.

Open Access This article is licensed under a Creative Commons Attribution 4.0 International License, which permits use, sharing, adaptation, distribution and reproduction in any medium or format, as long as you give appropriate credit to the original author(s) and the source, provide a link to the Creative Commons licence, and indicate if changes were made. The images or other third party material in this article are included in the article's Creative Commons licence, unless indicated otherwise in a credit line to the material. If material is not included in the article's Creative Commons licence and your intended use is not permitted by statutory regulation or exceeds the permitted use, you will need to obtain permission directly from the copyright holder. To view a copy of this licence, visit <http://creativecommons.org/licenses/by/4.0/>.

References

- [1] Pokropivny V, Lohmus R, Hussainova I et al (2007) Introduction to nanomaterials and nanotechnology. Tartu University Press, Tartu (ISBN: 978-9949-11-741-3)
- [2] Pradeep T (2007) Nano: the essentials. Tata McGraw-Hill Education, New York
- [3] Khan FA (2020) Nanomaterials: types, classifications, and sources. Applications of nanomaterials in human health. Springer, Singapore, pp 1–13
- [4] Nikaeen G, Abbaszadeh S, Yousefinejad S (2020) Application of nanomaterials in treatment, anti-infection and detection of coronaviruses. *Nanomedicine* 15:1501–1512. <https://doi.org/10.2217/nmm-2020-0117>
- [5] Salem SS (2023) Application of Nano-materials. *Haematococcus*. Springer, Singapore, pp 149–163
- [6] Mandal G, Ganguly T (2011) Applications of nanomaterials in the different fields of photosciences. *Indian J Phys* 85:1229–1245. <https://doi.org/10.1007/s12648-011-0149-9>
- [7] Swapna MS, Raj V, Cabrera H, Sankararaman SI (2021) Thermal lensing of multi-walled carbon nanotube solutions as heat transfer nanofluids. *ACS Appl Nano Mater* 4:3416–3425. <https://doi.org/10.1021/acsanm.0c03219>
- [8] Gokul V, Swapna MS, Raj V et al (2021) Development of zinc oxide-multi-walled carbon nanotube hybrid nanofluid for energy-efficient heat transfer application: a thermal lens study. *Phys Fluids* 33:107108-1–107108-9. <https://doi.org/10.1063/5.0067041>
- [9] Mishra YK, Murugan NA, Kotakoski J, Adam J (2017) Progress in electronics and photonics with nanomaterials. *Vacuum* 146:304–307. <https://doi.org/10.1016/j.vacuum.2017.09.035>
- [10] Kadri E, Messaoudi O, Krichen M et al (2017) Optical and electrical properties of SiGe/Si solar cell heterostructures: ellipsometric study. *J Alloys Compd* 721:779–783. <https://doi.org/10.1016/j.jallcom.2017.06.025>
- [11] Balasingam SK, Sivalingam Nallathambi K, Abdul Jabbar MH et al (2019) Nanomaterials for electrochemical energy conversion and storage technologies. *J Nanomater* 2019:1–2. <https://doi.org/10.1155/2019/1089842>

- [12] Zhang Q, Uchaker E, Candelaria SL, Cao G (2013) Nanomaterials for energy conversion and storage. *Chem Soc Rev* 42:3127–3171. <https://doi.org/10.1039/c3cs00009e>
- [13] Kadri E, Dhahri K, Zaafour A et al (2017) Ac conductivity and dielectric behavior of a-Si:H/c-Si_{1-y} Gey/p-Si thin films synthesized by molecular beam epitaxial method. *J Alloys Compd* 705:708–713. <https://doi.org/10.1016/j.jallcom.2017.02.117>
- [14] Laudadio E, Mohebbi E, Pavoni E et al (2023) Density functional theory and molecular dynamics studies on electrical, mechanical, and thermal properties of TiO₂ nanoparticles interacting with poly lactic-co-glycolic acid. *Colloids Surf A Physicochem Eng Asp* 667:131388–1–131388-10. <https://doi.org/10.1016/j.colsurfa.2023.131388>
- [15] Mohammadzahari M, Jamehbozorgi S, Ganji MD et al (2023) Toward functionalization of ZnO nanotubes and monolayers with 5-aminolevulinic acid drugs as possible nanocarriers for drug delivery: a DFT based molecular dynamic simulation. *Phys Chem Chem Phys* 25:21492–21508. <https://doi.org/10.1039/D3CP01490H>
- [16] Cabrera H, Korte D, Budasheva H et al (2021) Through-plane and in-plane thermal diffusivity determination of graphene nanoplatelets by photothermal beam deflection spectrometry. *Materials* 14:7273-1–7273-17. <https://doi.org/10.3390/ma14237273>
- [17] Swapna MNS, Korte D, Sankararaman SI (2023) Solid-volume-fraction retained tailoring of thermal diffusivity of multiwalled carbon nanotube nanofluid: a photothermal investigation. *Phys Status Solidi* 220:2200797-1–2200797-10. <https://doi.org/10.1002/pssa.202200797>
- [18] Chrobak Ł, Maliński M (2019) On investigations of the optical absorption coefficient of gold and germanium implanted silicon with the use of the non-destructive contactless photo thermal infrared radiometry. *J Electron Mater* 48:5273–5278. <https://doi.org/10.1007/s11664-019-07333-0>
- [19] Soumya S, Arun Kumar R, Raj V et al (2021) Thermal diffusivity of molybdenum oxide nanowire film: a photothermal beam deflection study. *Opt Laser Technol* 139:106993-1–106993-6. <https://doi.org/10.1016/j.optlastec.2021.106993>
- [20] Maver U, Khanari K, Žižek M et al (2018) A combination of interdisciplinary analytical tools for evaluation of multilayered coatings on medical grade stainless steel for biomedical applications. *Eur J Pharm Biopharm* 128:230–246. <https://doi.org/10.1016/j.ejpb.2018.05.002>
- [21] Sell J (2012) Photothermal investigations of solids and fluids, 1st edn. Elsevier, Netherlands, pp 8–10
- [22] Bialkowski SE, Astrath NGC, Proskurnin MA (2019) Photothermal spectroscopy methods, 2nd edn. Wiley, New Jersey
- [23] Dadarlat D, Tripon C, White IR, Korte D (2022) Photopyroelectric spectroscopy and calorimetry. *J Appl Phys* 132:191101-1–191101-36. <https://doi.org/10.1063/5.0085594>
- [24] Bićanić D (1992) Photoacoustic and photothermal phenomena III, vol 69. Springer Series in Optical Sciences. Springer, Berlin, p 1–732
- [25] Kobylińska DK, Bukowski RJ, Bodzenta J, Kochowski S (2008) Thermal parameters of solids determination by the photodeflection method—theories and experiment comparison. *Opt Appl* 38:445–458
- [26] Chrobak MM (2018) Comparison of three nondestructive and contactless techniques for investigations of recombination parameters on an example of silicon samples. *Infrared Phys Technol* 91:1–7. <https://doi.org/10.1016/j.infrared.2018.03.013>
- [27] Franko M, Goljat L, Liu M et al (2023) Recent progress and applications of thermal lens spectrometry and photothermal beam deflection techniques in environmental sensing. *Sensors* 23:472-1–472-17. <https://doi.org/10.3390/s23010472>
- [28] Snook RD, Lowe RD (1995) Thermal lens spectrometry. A review. *Analyst* 120:2051–2068. <https://doi.org/10.1039/AN9952002051>
- [29] Raj V, Swapna MS, Sankararaman S (2018) Nondestructive radiative evaluation of adulteration in coconut oil. *Eur Phys J Plus* 133:544-1–544-10. <https://doi.org/10.1140/epjp/i2018-12357-6>
- [30] Liu M (2019) Influence of thermal conductivity on photothermal lens spectroscopy. *Thermochim Acta* 672:126–132. <https://doi.org/10.1016/j.tca.2018.12.022>
- [31] Franko M, Tran CD (2006) Thermal lens spectroscopy. In: Meyers RA (ed) *Encyclopedia of analytical chemistry: applications, theory and instrumentation*. Wiley Online Library, Chichester, pp 1249–1279
- [32] Khabibullin VR, Franko M, Proskurnin MA (2023) Accuracy of measurements of thermophysical parameters by dual-beam thermal-lens spectrometry. *Nanomaterials* 13:430-1–430-30. <https://doi.org/10.3390/nano13030430>
- [33] Silva R, de Araújo MAC, Jali P et al (2011) Thermal lens spectrometry: optimizing amplitude and shortening the transient time. *AIP Adv.* 1:022154-1–022154-12. <https://doi.org/10.1063/1.3609966>
- [34] Franko M (2008) Thermal lens spectrometric detection in flow injection analysis and separation techniques. *Appl Spectrosc Rev* 43:358–388. <https://doi.org/10.1080/05704920802108032>
- [35] Šikovec M, Franko M, Novič M, Veber M (2001) Effect of organic solvents in the on-line thermal lens spectrometric detection of chromium(III) and chromium(VI) after ion chromatographic separation. *J Chromatogr A* 920:119–125. [https://doi.org/10.1016/S0021-9673\(01\)00611-2](https://doi.org/10.1016/S0021-9673(01)00611-2)
- [36] Korte D, Grahovac A, Jerkič A, Vajdle O, Anojčić J, Guzsvány BB, Franko M (2017) Speciation and determination of ionic and trace-level colloidal silver in selected personal care products by thermal lens spectrometry. *Pharm Anal Acta* 09(1):1000573-1–1000573-10. <https://doi.org/10.4172/2153-2435.1000573>
- [37] Muzamil M, Khalid N, Aziz MD, Abbas SA (2014) Synthesis of silver nanoparticles by silver salt reduction and its characterization. *IOP Conf Ser Mater Sci Eng* 60:012034-1–012034-8. <https://doi.org/10.1088/1757-899X/60/1/012034>
- [38] Setoura K, Ito S, Yamada M et al (2017) Fabrication of silver nanoparticles from silver salt aqueous solution at water-glass interface by visible CW laser irradiation without reducing reagents. *J Photochem Photobiol A Chem* 344:168–177. <https://doi.org/10.1016/j.jphotochem.2017.05.002>
- [39] Prabhu S, Poulouse EK (2012) Silver nanoparticles: mechanism of antimicrobial action, synthesis, medical applications, and toxicity effects. *Int Nano Lett* 2:32-1–32-10. <https://doi.org/10.1186/2228-5326-2-32>
- [40] Irvani S, Korbekandi H, Mirmohammadi SV, Zolfaghari B (2014) Synthesis of silver nanoparticles: chemical, physical and biological methods. *Res Pharm Sci* 9:385–406
- [41] Li W, Calle L, Hanford A et al (2018) Investigation of silver biocide as a disinfection technology for spacecraft—an early literature review. In: 48th International conference on environmental systems, Albuquerque
- [42] Rezvani E, Rafferty A, McGuinness C, Kennedy J (2019) Adverse effects of nanosilver on human health and the environment. *Acta Biomater* 94:145–159. <https://doi.org/10.1016/j.actbio.2019.05.042>
- [43] Korte D, Tomsič G, Bratkich A et al (2019) Determination of iron in environmental water samples by FIA-TLS. *Acta Chim Slov* 66(4):814–820. <https://doi.org/10.17344/acsi.2018.4825>

- [44] Stegarescu A, Cabrera H, Budasheva H et al (2022) Synthesis and characterization of MWCNT-COOH/Fe₃O₄ and CNT-COOH/Fe₃O₄/NiO nanocomposites: assessment of adsorption and photocatalytic performance. *Nanomaterials* 12:3008–1–3008–19. <https://doi.org/10.3390/nano12173008>
- [45] Lung I, Stegarescu A, Opreș O, Soran M-L (2022) Testing MWCNT-COOH/Fe₃O₄ nanocomposite for the removal of ampicillin from synthetic aqueous solutions. *Stud Univ Babeș-Bolyai Chem* 67:141–149. <https://doi.org/10.24193/subbchem.2022.4.09>
- [46] Bellamkonda S, Thangavel N, Hafeez HY et al (2019) Highly active and stable multi-walled carbon nanotubes-graphene-TiO₂ nanohybrid: an efficient non-noble metal photocatalyst for water splitting. *Catal Today* 321–322:120–127. <https://doi.org/10.1016/j.cattod.2017.10.023>
- [47] Xu J, Wen Q, Zhang X et al (2021) One-step construction of multi-walled CNTs loaded with alpha-Fe₂O₃ nanoparticles for efficient photocatalytic properties. *Materials* 14:2820–1–2820–10. <https://doi.org/10.3390/ma14112820>
- [48] Fujishima A, Zhang X (2006) Titanium dioxide photocatalysis: present situation and future approaches. *C R Chim* 9:750–760. <https://doi.org/10.1016/j.crci.2005.02.055>
- [49] Qian R, Zong H, Schneider J et al (2019) Charge carrier trapping, recombination and transfer during TiO₂ photocatalysis: an overview. *Catal Today* 335:78–90. <https://doi.org/10.1016/j.cattod.2018.10.053>
- [50] Ebrahimpour Z, Pliekhova O, Cabrera H et al (2021) Photodegradation mechanisms of reactive blue 19 dye under UV and simulated solar light irradiation. *Spectrochim Acta Part A Mol Biomol Spectrosc* 252: 119481–1–119481–10. <https://doi.org/10.1016/j.saa.2021.119481>
- [51] Pliekhova O, Arčon I, Pliekhov O et al (2017) Cu and Zr surface sites in the photocatalytic activity of TiO₂ nanoparticles. *Environ Sci Pollut Res* 24:12571–12581. <https://doi.org/10.1007/s11356-016-7685-y>
- [52] Kalikeri S, Kamath N, Gadgil DJ, Shetty Kodialbail V (2018) Visible light-induced photocatalytic degradation of Reactive Blue-19 over highly efficient polyaniline-TiO₂ nanocomposite: a comparative study with solar and UV photocatalysis. *Environ Sci Pollut Res* 25:3731–3744. <https://doi.org/10.1007/s11356-017-0663-1>
- [53] Hwang YJ, Yang S, Lee H (2017) Surface analysis of N-doped TiO₂ nanorods and their enhanced photocatalytic oxidation activity. *Appl Catal B Environ* 204:209–215. <https://doi.org/10.1016/j.apcatb.2016.11.038>
- [54] Swapna MS, Raj V, Sankararaman S (2019) Allotropic transformation instigated thermal diffusivity of soot nanofluid: thermal lens study. *Phys Fluids* 31:117106–1–117106–8. <https://doi.org/10.1063/1.5124030>
- [55] Swapna MS, Sankararaman S (2017) Investigation of graphene oxide in diesel soot. *J Mater Sci Nanotechnol* 5:103–1–103–6. <https://doi.org/10.15744/2348-9812.5.103>
- [56] Murr LE, Guerrero PA (2006) Carbon nanotubes in wood soot. *Atmos Sci Lett* 7:93–95
- [57] Swapna MS, Sankararaman S (2020) Tuning the thermal diffusivity of the seed matter for enhanced biosynthesis: a thermal lens study. *Eur Phys J Plus* 135:224–1–224–14. <https://doi.org/10.1140/epjp/s13360-020-00253-7>
- [58] Sankararaman S (2022) How graph features decipher the soot assisted pigmental energy transport in leaves? A laser-assisted thermal lens study in nanobiophotonics. *Chin Phys B* 31:088201–1–088201–8. <https://doi.org/10.1088/1674-1056/ac6740>
- [59] Rydosz A (2022) *Diabetes without needles*. Academic Press, Elsevier
- [60] Djordjević KL, Markushev DK, Popović MN et al (2023) Photoacoustic characterization of TiO₂ thin-films deposited on silicon substrate using neural networks. *Materials* 16:2865–1–2865–16. <https://doi.org/10.3390/ma16072865>
- [61] Markezini MV, Cella N, Mansanares AM et al (1991) Open photoacoustic cell spectroscopy. *Meas Sci Technol* 2:396–401. <https://doi.org/10.1088/0957-0233/2/4/020>
- [62] Todorović DM, Rabasović MD, Markushev DD, Sarajlić M (2014) Photoacoustic elastic bending in thin film–substrate system: experimental determination of the thin film parameters. *J Appl Phys* 116:053506–1–053506–9. <https://doi.org/10.1063/1.4890346>
- [63] Jovančić N, Markushev DK, Markushev DD et al (2020) Thermal and elastic characterization of nanostructured Fe₂O₃ polymorphs and TiO₂-coated Fe₂O₃ using open photoacoustic cell. *Int J Thermophys* 41:90. <https://doi.org/10.1007/s10765-020-02669-w>
- [64] Todorovic-acute DM, Nikolic-acute PM, Bojicic-acute AI, Radulovic-acute KT (1997) Thermoelastic and electronic strain contributions to the frequency transmission photoacoustic effect in semiconductors. *Phys Rev B* 55:15631–15642. <https://doi.org/10.1103/PhysRevB.55.15631>
- [65] McDonald FA, Wetsel GC (1978) Generalized theory of the photoacoustic effect. *J Appl Phys* 49:2313–2322. <https://doi.org/10.1063/1.325116>
- [66] Barreca D, Carraro G, Gasparotto A et al (2013) Surface functionalization of nanostructured Fe₂O₃ polymorphs: from design to light-activated applications. *ACS Appl Mater Interfaces* 5:7130–7138. <https://doi.org/10.1021/am401475g>
- [67] Aleksic S, Markushev D, Pantic D et al (2016) Electro-acoustic influence of the measuring system on the photoacoustic signal amplitude and phase in frequency domain. *Facta Univ Ser Phys Chem Technol* 14:9–20. <https://doi.org/10.2298/FUPCT160109A>
- [68] Markushev DD, Ordonez-Miranda J, Rabasović MD et al (2015) Effect of the absorption coefficient of aluminium plates on their thermoelastic bending in photoacoustic experiments. *J Appl Phys* 117:245309–1–245309–8. <https://doi.org/10.1063/1.4922718>
- [69] Korte D, Carraro G, Fresno F, Franko M (2014) Thermal properties of surface-modified α - and ϵ -Fe₂O₃ photocatalysts determined by beam deflection spectroscopy. *Int J Thermophys* 35:2107–2114. <https://doi.org/10.1007/s10765-014-1739-5>
- [70] Swapna MS, Nampoori VPN, Sankararaman S (2018) Photoacoustics: a nondestructive evaluation technique for thermal and optical characterisation of metal mirrors. *J Opt* 47(3):405–411. <https://doi.org/10.1007/s12596-018-0471-0>
- [71] Lamastra FR, Grilli ML, Leahu G et al (2018) Photoacoustic spectroscopy investigation of zinc oxide/diatom frustules hybrid powders. *Int J Thermophys* 39:110–1–110–10. <https://doi.org/10.1007/s10765-018-2428-6>
- [72] De Angelis R, Melino S, Proposito P et al (2016) The diatom *Stauriosirella pinnata* for photoactive material production. *PLoS ONE* 11:e0165571–1–e0165571–17. <https://doi.org/10.1371/journal.pone.0165571>
- [73] Lamastra FR, Mori S, Cherubini V et al (2017) A new green methodology for surface modification of diatomite filler in elastomers. *Mater Chem Phys* 194:253–260. <https://doi.org/10.1016/j.matchemphys.2017.03.050>
- [74] Losic D, Mitchell JG, Voelcker NH (2006) Fabrication of gold nanostructures by templating from porous diatom frustules. *New J Chem* 30:908–914. <https://doi.org/10.1039/b600073h>

- [75] Li XD, Chen TP, Liu P et al (2013) Effects of free electrons and quantum confinement in ultrathin ZnO films: a comparison between undoped and Al-doped ZnO. *Opt Express* 21:14131–14138
- [76] Azmina MS, Md Nor R, Rafaie HA et al (2017) Enhanced photocatalytic activity of ZnO nanoparticles grown on porous silica microparticles. *Appl Nanosci* 7:885–892
- [77] Petronijevic E, Leahu G, Belardini A et al (2018) Photo-acoustic spectroscopy reveals extrinsic optical chirality in GaAs-based nanowires partially covered with gold. *Int J Thermophys* 39:1–9
- [78] Zelepukin IV, Mashkovich EA, Lipey NA et al (2022) Direct photoacoustic measurement of silicon nanoparticle degradation promoted by a polymer coating. *Chem Eng J* 430:132860-1–132860-12
- [79] Dubyk K, Pastushenko A, Nychporuk T et al (2019) Thermal conductivity of silicon nanomaterials measured using the photoacoustic technique in a piezoelectric configuration. *J Phys Chem Solids* 126:267–273. <https://doi.org/10.1016/j.jpcs.2018.12.002>
- [80] Touloukian YS, Powell RW, Ho CY, Klemens PG (1970) Thermophysical properties of matter—the TPRC data series. Volume 1. Thermal conductivity-metallic elements and alloys. Purdue University, Lafayette. Thermophysical and Electronic Properties Information Center
- [81] Okasha AM, Mohamed MB, Abdallah T et al (2010) Characterization of core/shell (Ag/CdSe) nanostructure using photoacoustic spectroscopy. *J Phys Conf Ser* 214012131-1–012131-4. <https://doi.org/10.1088/1742-6596/214/1/012131>
- [82] Efros AL, Efros AL (1982) Interband absorption of light in a semiconductor sphere. *Sov Phys Semicond* 16:772–775
- [83] Carbajal-Valdéz R, Rodríguez-Juárez A, Jiménez-Pérez JL et al (2019) Experimental investigation on thermal properties of Ag nanowire nanofluids at low concentrations. *Thermochim Acta* 671:83–88. <https://doi.org/10.1016/j.tca.2018.11.015>
- [84] Balderas-Lopez JA, Acosta-Avalos D, Alvarado JJ et al (1995) Photoacoustic measurements of transparent liquid samples: thermal effusivity. *Meas Sci Technol* 6:1163–1168. <https://doi.org/10.1088/0957-0233/6/8/011>
- [85] Choi SUS, Eastman JA (1995) Enhancing thermal conductivity of fluids with nanoparticles. Argonne National Lab., Lemont
- [86] Pedreira PRB, Hirsch L, Pereira JRD et al (2003) Temperature dependence of the thermo-optical properties of water determined by thermal lens spectrometry. *Rev Sci Instrum* 74:808–810. <https://doi.org/10.1063/1.1517161>
- [87] Jiménez-Pérez JL, Pincel PV, Cruz-Orea A, Correa-Pacheco ZN (2016) Thermal characterization of a liquid resin for 3D printing using photothermal techniques. *Appl Phys A* 122:556-1–556-5. <https://doi.org/10.1007/s00339-016-0088-6>
- [88] Cabrera H, Cordido F, Velásquez A et al (2013) Measurement of the Soret coefficients in organic/water mixtures by thermal lens spectrometry. *C R Méc* 341:372–377. <https://doi.org/10.1016/j.crme.2013.01.011>
- [89] Kumar P, Khan A, Goswami D (2014) Importance of molecular heat convection in time resolved thermal lens study of highly absorbing samples. *Chem Phys* 441:5–10. <https://doi.org/10.1016/j.chemphys.2014.06.008>
- [90] Astrath NGC, Astrath FBG, Shen J et al (2009) Arrhenius behavior of hydrocarbon fuel photochemical reaction rates by thermal lens spectroscopy. *Appl Phys Lett*. 95:191902-1–191902-3 <https://doi.org/10.1063/1.3258661>
- [91] Cruz RA, Marcano A, Jacinto C, Catunda T (2009) Ultrasensitive thermal lens spectroscopy of water. *Opt Lett* 34:1882–1884. <https://doi.org/10.1364/OL.34.001882>
- [92] Cabrera H, Sira E, Rahn K, García-Sucre M (2009) A thermal lens model including the Soret effect. *Appl Phys Lett* 94:051103-1–051103-3. <https://doi.org/10.1063/1.3078287>
- [93] Cassano CL, Mawatari K, Kitamori T, Fan ZH (2014) Thermal lens microscopy as a detector in microdevices. *Electrophoresis* 35:2279–2291. <https://doi.org/10.1002/elps.201300430>
- [94] Kitamori T (2019) Thermal lens microscope and microchip chemistry. *Bull Chem Soc Jpn* 92:469–473. <https://doi.org/10.1246/bcsj.20180276>
- [95] Smirnova A, Proskurnin MA, Mawatari K, Kitamori T (2012) Desktop near-field thermal-lens microscope for thermo-optical detection in microfluidics. *Electrophoresis* 33:2748–2751. <https://doi.org/10.1002/elps.201200065>
- [96] Liu M, Novak U, Plazl I, Franko M (2014) Optimization of a thermal lens microscope for detection in a microfluidic chip. *Int J Thermophys* 35:2011–2022. <https://doi.org/10.1007/s10765-013-1515-y>
- [97] Shimizu H, Mawatari K, Kitamori T (2009) Development of a differential interference contrast thermal lens microscope for sensitive individual nanoparticle detection in liquid. *Anal Chem* 81:9802–9806. <https://doi.org/10.1021/ac901888u>
- [98] Marcano AO, Rodríguez L, Melikechi N (2002) Thermal lensing in extended samples. *Appl Spectrosc* 56:1504–1507. <https://doi.org/10.1366/00037020260377832>
- [99] Georges J (1999) Advantages and limitations of thermal lens spectrometry over conventional spectrophotometry for absorbance measurements. *Talanta* 48:501–509. [https://doi.org/10.1016/S0039-9140\(98\)00242-2](https://doi.org/10.1016/S0039-9140(98)00242-2)
- [100] Abbas Ghaleb K, Georges J (2004) Investigation of the optimum optical design for pulsed-laser crossed-beam thermal lens spectrometry in infinite and finite samples. *Spectrochim Acta Part A Mol Biomol Spectrosc* 60:863–872. [https://doi.org/10.1016/S1386-1425\(03\)00311-1](https://doi.org/10.1016/S1386-1425(03)00311-1)
- [101] Chanlon S, Georges J (2002) Pulsed-laser mode-mismatched crossed-beam thermal lens spectrometry within a small capillary tube: effect of flow rate and beam offset on the photothermal signal. *Spectrochim Acta Part A Mol Biomol Spectrosc* 58:1607–1613. [https://doi.org/10.1016/S1386-1425\(01\)00612-6](https://doi.org/10.1016/S1386-1425(01)00612-6)
- [102] Seta N, Mawatari K, Kitamori T (2009) Individual nanoparticle detection in liquids by thermal lens microscopy and improvement of detection efficiency using a 1- μ m microfluidic channel. *Anal Sci* 25:275–278. <https://doi.org/10.2116/analsci.25.275>
- [103] Adhikari S, Spaeth P, Kar A et al (2020) Photothermal microscopy: imaging the optical absorption of single nanoparticles and single molecules. *ACS Nano* 14:16414–16445. <https://doi.org/10.1021/acsnano.0c07638>
- [104] Georges J (2008) Matrix effects in thermal lens spectrometry: influence of salts, surfactants, polymers and solvent mixtures. *Spectrochim Acta Part A Mol Biomol Spectrosc* 69:1063–1072. <https://doi.org/10.1016/j.saa.2007.07.062>
- [105] Shokoufi N, Hamdamali A (2010) Laser induced-thermal lens spectrometry in combination with dispersive liquid–liquid microextraction for trace analysis. *Anal Chim Acta* 681:56–62. <https://doi.org/10.1016/j.aca.2010.09.021>
- [106] Grishko VI, Tran CD, Duley WW (2002) Enhancement of the thermal lens signal induced by sample matrix absorption of the probe laser beam. *Appl Opt* 41:5814–5822. <https://doi.org/10.1364/AO.41.005814>
- [107] Šeděnková I, Taboubi O, Paúrová M et al (2023) Influence of the type and concentration of oxidant on the photoacoustic response of polypyrrole nanoparticles for potential bioimaging applications. *Synth Met* 292:117218-1–117218-9. <https://doi.org/10.1016/j.synthmet.2022.117218>

- [108] Sim JY, Ahn C-G, Jeong E-J, Kim BK (2018) In vivo microscopic photoacoustic spectroscopy for non-invasive glucose monitoring invulnerable to skin secretion products. *Sci Rep* 8:1059-1–1059-1. <https://doi.org/10.1038/s41598-018-19340-y>
- [109] Jin Y, Yin Y, Li C et al (2022) Non-invasive monitoring of human health by photoacoustic spectroscopy. *Sensors* 22:1155-1–1155-14. <https://doi.org/10.3390/s22031155>
- [110] Schmid T (2006) Photoacoustic spectroscopy for process analysis. *Anal Bioanal Chem* 384:1071–1086. <https://doi.org/10.1007/s00216-005-3281-6>
- [111] Zhang B, Chen K, Chen Y et al (2020) High-sensitivity photoacoustic gas detector by employing multi-pass cell and fiber-optic microphone. *Opt Express* 28:6618–6630. <https://doi.org/10.1364/OE.382310>
- [112] Aleksić SM, Markushev DK, Markushev DD et al (2022) Photoacoustic analysis of illuminated Si–TiO₂ sample bending along the heat-flow axes. *SILICON* 14:9853–9861. <https://doi.org/10.1007/s12633-022-01723-6>
- [113] Abad B, Borca-Tasciuc D-A, Martin-Gonzalez MS (2017) Non-contact methods for thermal properties measurement. *Renew Sustain Energy Rev* 76:1348–1370. <https://doi.org/10.1016/j.rser.2017.03.027>
- [114] Cox BT, Arridge SR, Köstli KP, Beard PC (2006) Two-dimensional quantitative photoacoustic image reconstruction of absorption distributions in scattering media by use of a simple iterative method. *Appl Opt* 45:1866–1875. <https://doi.org/10.1364/AO.45.001866>
- [115] Hysi E, Moore MJ, Strohm EM, Kolios MC (2021) A tutorial in photoacoustic microscopy and tomography signal processing methods. *J Appl Phys.* 124:141102-1–141102-22. <https://doi.org/10.1063/5.0040783>
- [116] Litvinenko S, Lishchuk P, Lysenko V, Isaiev M (2021) Bi-modal photothermal/optical microscopy for complementary bio-imaging with high resolution and contrast. *Appl Phys B* 127:139-1–139-5. <https://doi.org/10.1007/s00340-021-07686-7>
- [117] Burbelo RM, Kuz'mich AG, Kucherov IY (1999) Photothermal and photoelectric microscopy of silicon. *Semiconductors* 33:630–635. <https://doi.org/10.1134/1.1187744>
- [118] Proskurnin MA, Usoltseva LO, Volkov DS et al (2021) Photothermal and heat-transfer properties of aqueous detonation nanodiamonds by photothermal microscopy and transient spectroscopy. *J Phys Chem C* 125:7808–7823. <https://doi.org/10.1021/acs.jpcc.0c09329>
- [119] Dubyk K, Chepela L, Alekseev S et al (2020) Some types of carbon-based nanomaterials as contrast agents for photoacoustic tomography. *J Nano-Electron Phys* 12:04033-1–04033-6. [https://doi.org/10.21272/jnep.12\(4\).04033](https://doi.org/10.21272/jnep.12(4).04033)

Publisher's Note Springer Nature remains neutral with regard to jurisdictional claims in published maps and institutional affiliations.